1 **Title:** Cytopurgosis: an export mechanism for organelle clearance that compensates for

2 impaired lysosomal degradation

3 **Authors**: Lishuan Wu[1,2,3,4], Yiming Lei[1,2,3,4] and Hongyun Tang[1,2,3,5]*

4 [1]State Key Laboratory of Gene Expression, School of Life Sciences, Westlake University,

5 Hangzhou 310024, China

6 [2]Westlake Laboratory of Life Sciences and Biomedicine, Hangzhou 310024, China.

7 [3]Institute of Biology, Westlake Institute for Advanced Study, Hangzhou 310024, China.

8 [4]These authors contributed equally

9 [5]Lead contact

10 *Correspondence: tanghongyun@westlake.edu.cn

11 **Keywords:** organelle-enriched extracellular vesicles; organelle expulsion; lysosomal

12 quality control; organelle removal; lysosomal overload; large extracellular vesicle

13 **ABSTRACT**

14   Cells must eliminate various unwanted organelles to maintain homeostasis, yet

15 how they achieve this when their primary degradation system, the lysosome, is impaired

16 remains poorly understood. Here, we discover cytopurgosis, a lysosome-independent

17 organelle-removal pathway that expels multiple organelles, including entire lysosomes,

18 within large extracellular vesicles that we termed "purgasomes". Cytopurgosis

19 transitions from a basal process to a robust stress response under conditions of

20 lysosomal overload, including in a genetic model of Niemann-Pick type C1 disease.

21 Mechanistically, this lysosomal stress reduces plasma membrane $PI(4,5)P_2$ levels,

22 triggering phosphatidylethanolamine externalization, which drives purgasome

23 formation through plasma membrane budding. Importantly, cytopurgosis exhibits cargo

24 selectivity, enabling cells to selectively sort and eject overloaded lysosomes dependent

25 on RAB-7 and UNC-116/Kinesin-1, which is crucial for preserving lysosomal

26 homeostasis. Our findings establish cytopurgosis as a fundamental organelle disposal

27 pathway that complements intracellular degradation and reveal purgasome-mediated

28 lysosome export as a previously-unknown lysosomal quality control mechanism.

29

INTRODUCTION

The removal of surplus or damaged organelles is essential for maintaining cellular homeostasis and viability by regulating both organelle quantity and quality (Anding and Baehrecke, 2017; Khaminets et al., 2015; Kurihara et al., 2012; Liu et al., 2023; Sandoval et al., 2008; Youle and Narendra, 2010). Although lysosome-dependent selective autophagy is widely regarded as the primary mechanism for eliminating organelles such as mitochondria and ER (Khaminets et al., 2015; Li et al., 2021; Sica et al., 2015; Sun et al., 2024; Youle and Narendra, 2010), this mechanism does not explain organelle turnover in lysosome-deficient cells or under conditions of lysosomal dysfunction (Liu et al., 2023), necessitating the existence of lysosome-independent mechanisms of organelle removal. Failures in organelle removal are implicated in developmental defects and aging (Anding and Baehrecke, 2017; Li et al., 2021); therefore, uncovering such alternative clearance pathways is imperative.

One such potential pathway is the extracellular release of organelles. Recent studies have demonstrated that cells can regulate mitochondrial content and quality by shedding mitochondria through various extracellular vesicles (EVs) (Jeppesen et al., 2025; Jiao et al., 2021; Liu et al., 2023; Melentijevic et al., 2017), suggesting cell's capacity for exporting organelles. However, it remains to be determined whether extracellular release represents a broad mechanism capable of clearing various types of organelles, which may complement selective autophagy, particularly when intracellular degradation is insufficient. Such a compensatory pathway would be particularly critical when lysosomal degradation is overwhelmed, as occurs under conditions of lysosomal substrate overload, a common feature of aging and lysosomal storage disorders (LSDs) (Eguchi et al., 2018; Platt et al., 2018). While cells can repair or degrade membrane-damaged lysosomes through mechanisms like membrane repair and lysophagy (Hung et al., 2013; Maejima et al., 2013; Radulovic et al., 2018; Skowyra et al., 2018; Tan and Finkel, 2022), the mechanisms by which overloaded lysosomes are resolved remain unknown. Therefore, a central question is whether cells can preserve homeostasis by

58   expelling entire overloaded lysosomes along with other dysfunctional organelles.

59   In this *in vivo* study, we uncover a pathway for organelle removal that operates

60   independently of lysosomal degradation, using *C. elegans* coelomocytes. We identify a

61   previously unrecognized class of large EV, which we term "purgasomes," capable of

62   expelling diverse organelles, including lysosomes, mitochondria, ER, and Golgi.

63   Purgasome biogenesis, cytopurgosis, occurs at a basal level but is markedly upregulated

64   upon autophagy impairment or lysosomal overload, revealing a compensatory

65   relationship with intracellular degradation pathways. Mechanistically, lysosomal stress

66   reduces plasma membrane $PI(4,5)P_2$ levels, promoting phosphatidylethanolamine

67   externalization and driving purgasome formation through a plasma membrane budding

68   process. Furthermore, overloaded lysosomes are selectively targeted for expulsion via

69   purgasomes requiring the GTPase RAB-7 and the motor protein UNC-116 (Kinesin-1).

70   This selective removal is critical for maintaining intracellular lysosomal function.

71   Collectively, our findings establish cytopurgosis as a fundamental organelle clearance

72   mechanism that operates in parallel to intracellular degradation process, with

73   purgasome-mediated lysosome expulsion serving as a stress-responsive quality control

74   pathway essential for cellular and lysosomal homeostasis.

75   **RESULTS**

76   **Cells expel various organelles through a distinct extracellular vesicle termed the**

77   **"purgasome", which is markedly enhanced by lysosomal overload stress**

78   To investigate lysosome-independent organelle clearance, we explored whether

79   cells can actively eject diverse organelles when lysosomal degradation is overwhelmed

80   by substrate overload. Using *C. elegans* as a model organism, we generated transgenic

81   strains to induce lysosomal substrate overload specifically in coelomocytes, cells with

82   high endocytic activity that internalize proteins secreted into the body cavity, thereby

83   enabling targeted lysosomal accumulation. We employed two intestinal secretion

84   strategies using the *nhx-2* promoter (Nehrke and Melvin, 2002) to drive protein release

85   from the intestine into the body cavity: (1) conventional secretion of an intestine-

86   specific expressed signal peptide-tagged wrmScarlet from an *Is[nhx-*

87 *2p::sp::wrmScarlet]* transgene (Fig. S1A), and (2) lysosomal exocytosis, involving the

88 fusion of lysosomal membrane with the plasma membrane, to secrete intestine-specific

89 expressed wrmScarlet fusion with lysosome lumen-localized CPL-1 cathepsin from an

90 *Is[nhx-2p::CPL-1::wrmScarlet]* transgene (Fig. 1A and B). As anticipated, the

91 intestine-secreted proteins from both approaches were internalized by coelomocytes

92 (Fig. 1C and D; S1B) and targeted to the lysosomal lumen, as confirmed by the

93 wrmScarlet signal enveloped by the GFP-tagged lysosome membrane protein 1 (LMP-

94 1::GFP) expressed in coelomocytes (Fig. 1E and F; S1C and D). Consistent with

95 lysosomal exocytosis as the secretion mechanism for CPL-1::wrmScarlet, RNAi

96 knockdown of *rab-10*, which encodes a small GTPase required for lysosome exocytosis

97 (Eguchi et al., 2018), led to the accumulation of CPL-1::wrmScarlet within intestinal

98 lysosomes marked by LAAT-1::GFP (Fig. S1E and F) and a reduction of CPL-

99 1::wrmScarlet signals in coelomocytes (Fig. S1G). Notably, wrmScarlet accumulation

100 in coelomocyte lysosomes was substantially higher in *Is[nhx-2p::CPL-1::wrmScarlet]*

101 animals compared to *Is[nhx-2p::sp::wrmScarlet]* worms (Fig. S1H). This difference

102 was further evidenced by the observation that the lysosomal wrmScarlet accumulation

103 in coelomocytes from the *Is[nhx-2p::CPL-1::wrmScarlet]* strain is so strong that

104 spectral spillover into the BFP and GFP detection channels is readily detectable (Fig.

105 S1J), whereas such spillover is observed in only a minor fraction of *Is[nhx-*

106 *2p::sp::wrmScarlet]* worms (Fig. S1I and S1K). Thus, we successfully established

107 transgenic models of lysosomal substrate overload in coelomocytes.

108 Strikingly, confocal microscopy analyses revealed that in *Is[nhx-2p::CPL-*

109 *1::wrmScarlet]* worms, coelomocytes export CPL-1::wrmScarlet-labeled lysosomes

110 within large EVs with an average diameter of approximately 5 µm (Fig. 1G and H).

111 These EVs originated from the coelomocyte plasma membrane, as evidenced by the

112 presence of the coelomocyte-expressed cell surface marker GFP::MCA-3 on the

113 membranes of all lysosome-embedded EVs (Fig. 1G and I). Correlative light and

114 electron microscopy (CLEM) confirmed that CPL-1::wrmScarlet signals were

115 exclusively localized within lysosomes and that these EVs contained wrmScarlet-laden

116 lysosomes (Fig. 1J and K). Quantitative analysis of all six coelomocytes in day-3 adult

117   worms showed that over 95% of *Is[nhx-2p::CPL-1::wrmScarlet]* animals produced

118   lysosome-carrying EVs (Fig. 1L), averaging approximately five such EVs per worm

119   (Fig. 1M). In contrast, only 12% of *Is[nhx-2p::sp::wrmScarlet]* worms generated EVs

120   containing lysosomes (Fig. S1K–M), with an average of 0.22 lysosome-carrying EVs

121   per worm (Fig. S1N), consistent with the milder lysosomal burden in these animals (Fig.

122   S1H–J). Moreover, coelomocytes accumulating wrmScarlet fused to catalytically

123   inactive CPL-1(C144A) in *Is[nhx-2p::CPL-1(C144A)::wrmScarlet]* worms (Xu et al.,

124   2014) displayed levels of lysosomal expulsion comparable to those observed in

125   coelomocytes accumulating wrmScarlet fused to wild-type CPL-1 in *Is[nhx-2p::CPL-*

126   *1::wrmScarlet]* worms (Fig. S1O–Q), further supporting the trigger for this lysosome

127   expulsion is the physical accumulation of tagged-wrmScarlet substrate rather than CPL-

128   1 enzymatic activity. Notably, even under homeostatic conditions without exogenous

129   lysosomal loading, low-level lysosome export via EVs was observed in coelomocytes,

130   with about 5% of wild-type worms expressing LMP-1::GFP exhibiting lysosome export

131   (Fig. 1L) and an average of 0.05 lysosome-carrying EVs per worm (Fig. 1M). Thus,

132   this expulsion mechanism operates at a basal level during homeostasis but is

133   dramatically amplified under lysosomal overload.

134   We then sought to determine if this lysosome expulsion pathway is a general

135   response to impaired intracellular degradation. Indeed, beyond lysosomal overload,

136   inhibition of autophagosome initiation via RNAi targeting *atg-1/ULK1 and epg-*

137   *7/FIP200*, or autophagosome expansion via RNAi targeting *atg-16.2/ATG16* in wild-

138   type worms with LMP-1::GFP-labeled lysosomes also increased lysosome export, with

139   27%, 27%, and 25% of worms showing lysosome export (Fig. 1N) and an average of

140   0.65, 0.68, and 0.64 lysosome-carrying EVs per worm (Fig. 1O), respectively. The more

141   pronounced lysosome expulsion observed with lysosomal overload of CPL-

142   1::wrmScarlet, compared to impaired autophagosome function, is consistent with that

143   lysosomes mediate both autophagosome-dependent and autophagosome-independent

144   clearance of organelles. Together, these findings demonstrate the existence of a basal

145   organelle export pathway that is strongly upregulated when intracellular degradation

146   via lysosomes or autophagy is compromised.

147   A key question was whether these large EVs were selective for lysosomes or

148 represented a bulk disposal pathway for diverse organelles. As the *Is[nhx-2p::CPL-*

149 *1::wrmScarlet]* transgene resulted in the most pronounced generation of lysosomes-

150 carrying EVs, we used this strain for further characterization. Strikingly, our

151 transmission electron microscopy (TEM) analyses revealed lysosomes, mitochondria,

152 ER, and Golgi apparatus within these large EVs (Fig. 1P-V), demonstrating their roles

153 in releasing various types of organelles (Fig. 1W). Moreover, the derivation of EV

154 membranes from the coelomocyte plasma membrane (Fig. 1G) indicates that these

155 vesicles form through ectocytosis rather than exocytosis (Fig. 1W). The ability of these

156 vesicles to export diverse organelles via ectocytosis identifies them as a previously

157 unrecognized subcellular structure, which we term "purgasome," and the process of its

158 generation as "cytopurgosis". Collectively, our results define cytopurgosis as a

159 lysosome-independent mechanism for the bulk removal of diverse organelles via

160 ectocytosis (Fig. 1W).

161 **Cytopurgosis is a unique process of organelle ectocytosis characterized by PE**

162 **externalization-dependent plasma membrane budding**

163   By investigating the morphologic features of forming purgasomes and the genetic

164 basis of purgasome biogenesis, we determined that cytopurgosis occurs through a

165 plasma membrane budding process. Firstly, microscopic analyses revealed the forming

166 purgasome as a plasma membrane-derived bud containing CPL-1::wrmScarlet-labeled

167 lysosomes (Fig. 2A-C). Furthermore, genetic requirement experiments also indicate

168 this budding model. Specifically, RNAi against *tat-5*, which encodes a lipid flippase

169 responsible for maintaining phosphatidylethanolamine (PE) in the inner leaflet and is

170 known to repress membrane budding (Beer et al., 2018), enhanced purgasome

171 production in the *Is[nhx-2p::CPL-1::wrmScarlet]* animals, from 5.5 to 8.4 purgasomes

172 per worm (Fig. 2D-E). In contrast, activating TAT-5 via the *pad-1(ju1806)* gain-of-

173 function mutation (Park et al., 2024) suppressed purgasome formation induced by

174 lysosomal accumulation of CPL-1::wrmScarlet (Fig. 2F and G). Unfortunately, likely

175 due to phototoxicity, purgasome generation was inhibited when performing live

176 imaging of *Is[nhx-2p::CPL-1::wrmScarlet]* worms, which prevented us from capturing

177 the dynamics of cytopurgosis. Collectively, purgasomes are large, organelle-enriched

178 extracellular vesicles produced via plasma membrane budding, which is regulated by

179 TAT-5.

180   Furthermore, purgasomes fundamentally differ from currently known large EVs

181 in their generation mechanisms. Specifically, unlike migrasomes, exophers, and

182 blebbisomes, which involve retraction fibers, thin fibers, or membrane nanotubes,

183 respectively, for their formation (Jeppesen et al., 2025; Ma et al., 2014; Melentijevic et

184 al., 2017), no such fiber structures are observed for the forming purgasomes (Fig. 2A-

185 C and S2A). Moreover, the generation of migrasomes and blebbisomes depends on cell

186 migration, whereas purgasomes can be produced by non-motile coelomocytes.

187 Blebbisome formation requires myosin IIB (the homolog of *C. elegans* NMY-2)

188 (Jeppesen et al., 2025), and exopher formation depends on POD-1 and EMB-8

189 (Melentijevic et al., 2017; Turek et al., 2021), whereas purgasome formation is not

190 inhibited by *nmy-2* or *pod-1* RNAi and is even slightly enhanced upon *emb-8*

191 knockdown (Fig. S2 B-D). Additionally, purgasomes differ from mitophers (~720 nm),

192 which selectively export mitochondria (Liu et al., 2023), by encapsulating diverse

193 organelles such as lysosomes, ER, mitochondria, and Golgi apparatus (Fig. 1Q-W), and

194 by exhibiting a larger size (Fig. 1H). These distinct genetic and cellular requirements

195 confirm that purgasomes are a unique class of EV mediating expulsion of various

196 organelles via ectocytosis.

197 **Cytopurgosis selectively exports lysosomes with impaired degradation capacity**

198 **and is enhanced by the LSDs-related *ncr-1/NPC1(lf)* mutation**

199   Given that lysosomal overload enhances purgasome-mediated lysosome expulsion

200 (Fig. 1L and M), we hypothesized that cytopurgosis functions as a quality control

201 pathway that selectively targets damaged organelles during cellular stress, analogous to

202 autophagy. Indeed, lysosomes within forming purgasomes were overloaded, exhibiting

203 stronger accumulation of the CPL-1::wrmScarlet substrate and increased size compared

204 to lysosomes retained in coelomocytes (Fig. 3A–D). Intriguingly, in contrast to those in

205 forming purgasomes, lysosomes within released purgasomes displayed reduced CPL-

206   1::wrmScarlet signal and smaller sizes relative to their intracellular counterparts (Fig.

207   S3A-C). These findings suggest that lysosomes progressively lose integrity following

208   purgasome release, leading to reduced substrate retention, contrasting with the

209   pronounced substrate accumulation observed in lysosomes within forming purgasomes.

210   To provide evidence for this potential lysosomal leakage in the purgasomes, we

211   employed the overexpression of GFP-fused galectin-3 (GFP::Gal3), previously shown

212   to promote lysosomal membrane repair after lysosomal membrane permeabilization

213   (Jia et al., 2020). Upon overexpression of GFP::Gal3, increased- CPL-1::wrmScarlet

214   signal intensity and enlarged lysosomal size were again observed within released

215   purgasomes, surpassing levels observed in intracellular lysosomes (Fig. S3D–F).

216   Together, these results demonstrate that compromised lysosomes are selectively

217   exported by cytopurgosis during lysosomal overload.

218   If cytopurgosis indeed preferentially exports overloaded lysosomes under

219   lysosomal stress, the degree of CPL-1::wrmScarlet lysosomal accumulation should

220   correlate positively with the extent of lysosome expulsion. To test this, we generated a

221   second *Is[nhx-2p::CPL-1::wrmScarlet]* transgene (line #2), which exhibited lower

222   lysosomal accumulation of CPL-1::wrmScarlet in the coelomocytes compared to the

223   first transgene (line #1) shown in Figure 1G (Fig. 3E and F). Consistent with our

224   hypothesis, transgenic line #2 produced fewer purgasomes than line #1 (Fig. 3G). This

225   reduced expulsion of lysosomes in response to lower lysosomal substrate accumulation

226   further supports that cytopurgosis facilitates the removal of compromised lysosomes

227   under lysosomal overload.

228   In addition to lysosomal protein substrate overload resulting from the

229   aforementioned transgenes, we investigated whether a genetic mutation in Niemann-

230   Pick type C1 (*NPC1*), associated with lysosomal storage disorders (LSDs) and

231   characterized by lysosomal cholesterol accumulation and impaired lysosomal function

232   (Lim et al., 2019; Platt et al., 2018), could promote lysosome expulsion via cytopurgosis.

233   To assess this, we examined the effect of a loss-of-function mutation in *ncr-1*, the *C.*

234   *elegans* ortholog of human NPC1, on lysosomal expulsion. As expected, introducing

235   the *ncr-1* mutation into *Is[nhx-2p::CPL-1::wrmScarlet]* worms resulted in a significant

236　increase in CPL-1::wrmScarlet accumulation within coelomocyte lysosomes (Fig. 3H

237　and I). Notably, the *ncr-1(lf)* mutation further enhanced purgasome-mediated lysosomal

238　expulsion in these worms (Fig. 3J). These findings demonstrate that cytopurgosis

239　responds to lysosomal overload not only from increased endocytic uptake but also from

240　genetic perturbations linked to LSDs, highlighting cytopurgosis as a stress-responsive

241　pathway for organelle clearance.

242　　　　Notably, our TEM analyses revealed that other organelles within purgasomes also

243　exhibited aberrant morphologies, including fragmented and clustered ER, irregular

244　mitochondrial shapes, and dilated Golgi structures, compared to their intracellular

245　counterparts (Fig. 1P–V). These observations suggest that cytopurgosis mediates the

246　selective export of multiple types of damaged organelles under lysosomal stress. The

247　coordinated expulsion of diverse stressed organelles aligns with the idea that when

248　lysosome-dependent degradation is impaired, cells rely on purgasome-mediated

249　extrusion as an alternative mechanism for organelle removal. Collectively, our data

250　indicate that under lysosomal stress, cytopurgosis selectively eliminates lysosomes with

251　compromised degradative capacity as well as other damaged organelles.

252　Lysosomal overload stress promotes purgasome formation by reducing plasma

253　membrane PI(4,5)P$_2$ levels

254　　　　Our data indicated that purgasome formation requires two coordinated processes:

255　remodeling of the plasma membrane to generate extracellular vesicles and the selective

256　loading of organelles, such as stressed lysosomes, into the forming EVs. To elucidate

257　how lysosomal stress triggers the change in plasma membrane to facilitate purgasome

258　formation, we first assessed levels of phosphatidylinositol 4,5-bisphosphate [PI(4,5)P$_2$],

259　the most abundant phosphoinositide on the cell surface. Using a well-established

260　reporter consisting of a GFP-tagged Pleckstrin Homology (PH) domain (PH-GFP)

261　(Bednarek et al., 2007), we observed a marked reduction in PH-GFP localization to the

262　plasma membrane of coelomocytes upon lysosomal overloading with CPL-

263　1::wrmScarlet (Fig. 4A and B), indicating that lysosomal overload stress reduces

264　PI(4,5)P$_2$ levels at the plasma membrane. Importantly, this reduction in PI(4,5)P$_2$

265   facilitates purgasome formation, as RNAi knockdown of the PI(4,5)P$_2$ biosynthesis

266   enzyme PPK-1 enhanced purgasome generation in *Is[nhx-2p::CPL-1::wrmScarlet]*

267   worms (Fig. 4C). Conversely, overexpression of PPK-1 specifically in coelomocytes,

268   using the promoter of *unc-122*, decreases the generation of lysosome-containing

269   purgasomes in worms with CPL-1::wrmScarlet-induced lysosomal overload (Fig. 4D).

270   Strikingly, even in the absence of lysosomal stress, *ppk-1* knockdown, resulting in

271   significantly reduced plasma membrane PI(4,5)P$_2$ levels (Fig. 4E and F), increased the

272   number of purgasomes derived from the coelomocytes (Fig. 4E and G). Thus, a

273   decrease in plasma membrane PI(4,5)P$_2$ is sufficient to induce purgasome formation.

274   Furthermore, consistent with a role of PPK-1 in repressing cytopurgosis, RNAi

275   against *arf-6*, a gene required for the localization of PPK-1 onto the plasma membrane

276   (Brown et al., 2001) (Fig. 4H and I) , elevated purgasome-mediated lysosome expulsion

277   in *Is[nhx-2p::CPL-1::wrmScarlet]* worms (Fig. 4J; S4A). Conversely, overexpression

278   of ARF-6 in coelomocytes was able to reduce the generation of lysosome-embedded

279   purgasomes induced by lysosomal CPL-1::wrmScarlet accumulation (Fig. 4K; S4B).

280   Collectively, lysosomal overloading stress leads to a decrease in plasma membrane

281   PI(4,5)P$_2$ levels, thereby promoting purgasome generation.

282   **PI(4,5)P$_2$ reduction triggers PE externalization to drive purgasome formation**

283   We subsequently investigated the mechanism by which lysosomal stress-induced

284   reduction of PI(4,5)P$_2$ facilitates purgasome generation. Given that *tat-5* RNAi,

285   disrupting the lipid flippase responsible for maintaining PE in the inner leaflet of the

286   plasma membrane, enhances cytopurgosis (Fig. 2D and E), we tested the potential

287   involvement of PE externalization, which has been suggested to alter plasma membrane

288   curvature and promote vesicle formation (Wehman et al., 2011). To assess PE

289   externalization, we used duramycin staining (Park et al., 2024), as demonstrated by the

290   robust labeling of the plasma membrane in coelomocytes of *tat-5*(RNAi)-treated worms

291   compared to controls (Fig. S4C-E). Strikingly, in *Is[nhx-2p::CPL-1::wrmScarlet]*

292   animals, duramycin staining showed clear PE externalization on both the plasma

293   membrane of coelomocytes and the membranes of purgasomes (Fig. 4L-O), in contrast

294 to the unstressed worms lacking CPL-1::wrmScarlet accumulation (Fig. 4L and O).

295 Therefore, lysosomal overload stress induces PE externalization at the plasma

296 membrane. This result, combined with the enhancement of cytopurgosis by *tat-5(RNAi)*

297 and its inhibition upon TAT-5 activation by *pad-1(gf, ju1806)* (Fig. 2D-G), supports that

298 PE externalization mediates the effect of lysosomal overload stress in promoting

299 purgasome formation.

300 Next, to determine whether reduced $PI(4,5)P_2$ is sufficient to drive PE

301 externalization in the absence of lysosomal stress, we examined PE exposure following

302 *ppk-1(RNAi)* in wild-type worms. Indeed, *ppk-1* knockdown led to prominent PE

303 externalization, as evidenced by duramycin staining on the plasma membrane of

304 coelomocytes (Fig. 4P-R). Additionally, our earlier results showed that reducing

305 $PI(4,5)P_2$ by *ppk-1(RNAi)* was able to promote purgasome formation in the absence of

306 lysosomal stress (Fig. 4E-G). Altogether, our results indicate that lysosomal substrate

307 overload reduces plasma membrane $PI(4,5)P_2$, thereby promoting PE externalization

308 and facilitating purgasome formation, which provides an effective route for the export

309 of stressed lysosomes.

The sorting of overloaded lysosomes into purgasomes is mediated by RAB-7

311 Next, to exemplify the mechanisms underlying the preferential expulsion of

312 dysfunctional organelles via purgasomes, we investigated how overloaded lysosomes

313 are selectively recognized. Given the critical role of Rab GTPases as key regulators of

314 organelle trafficking (Stenmark, 2009), we focused initially on RAB-7, known to

315 localize to the lysosomal membrane and regulate lysosomal dynamics (Cabukusta and

316 Neefjes, 2018). Using a GFP::RAB-7 reporter, we observed a marked increase in RAB-

317 7 levels on lysosomes within purgasomes compared to intracellular lysosomes in the

318 coelomocytes of *Is[nhx-2p::CPL-1::wrmScarlet]* worms (Fig. 5A and B). Furthermore,

319 *rab-7* knockdown significantly reduced lysosome expulsion induced by CPL-

320 1::wrmScarlet-mediated lysosomal overload (Fig. 5C). Similarly, expression of a

321 dominant-negative RAB-7 (T22N) variant specifically in coelomocytes suppressed

322 lysosome ectocytosis in *Is[nhx-2p::CPL-1::wrmScarlet]* worms (Fig. 5D). These

323   findings, combined with our earlier observation that lysosomes with greater substrate

324   accumulation are preferentially transported outward (Fig. 3A-D), indicate that

325   increased RAB-7 localization on overloaded lysosomes is crucial for their selective

326   export through cytopurgosis.

327   We next evaluated whether RAB-7 overexpression in coelomocytes by using the

328   *unc-122* promoter could enhance lysosome expulsion via cytopurgosis. Consistent with

329   the known role of RAB-7 in promoting lysosomal fusion (Hu et al., 2006), RAB-7

330   overexpression led to enlarged lysosomes in nearly 70% of coelomocytes (Fig. 5E and

331   F; S5A). However, this level of RAB-7 overexpression instead repressed lysosome

332   expulsion in *Is[nhx-2p::CPL-1::wrmScarlet]* worms (Fig. 5H), likely due to the

333   difficulty in translocating oversized lysosomes. Supporting this notion, the *Is[nhx-*

334   *2p::CPL-1::wrmScarlet]* worms treated with RNAi against *agef-1*, which encodes a

335   protein required for lysosomal fission (Tang et al., 2012), exhibited increased lysosome

336   size (Fig. S5B) and reduced lysosome expulsion (Fig. S5C). Therefore, to uncouple

337   RAB-7's role in expulsion from its function in lysosomal fusion, we utilized the RAB-

338   7-overexpressing transgene in a heterozygous state, which did not induce lysosomal

339   enlargement in *Is[nhx-2p::CPL-1::wrmScarlet]* worms (Fig. 5E and G). Strikingly,

340   heterozygous RAB-7 overexpression could significantly enhance purgasome-mediated

341   lysosome expulsion in *Is[nhx-2p::CPL-1::wrmScarlet]* worms (Fig. 5H). Collectively,

342   our results indicate that the selective increase of RAB-7 on overloaded lysosomes is

343   critical for their preferential extracellular disposal through cytopurgosis.

344   **The selective translocation of overloaded lysosomes into purgasomes is mediated**

345   **by the Kinesin UNC-116/Kinesin1**

346   To elucidate how the increase of RAB-7 on overloaded lysosomes drives their

347   outward translocation into purgasomes, we investigated the potential involvement of

348   motor proteins. Kinesin motors mediate anterograde transport; therefore, we first

349   conducted genetic analyses to examine the effects of 16 kinesin genes on cytopurgosis

350   in *Is[nhx-2p::CPL-1::wrmScarlet]* worms (Fig. S6A and B). The results revealed that

351   knockout of *unc-116*, the ortholog of mammalian KIF5/Kinesin1, showed the strongest

inhibitory effect on lysosomal expulsion via purgasomes (Fig. 6A; S6A and B). Further supporting the role of UNC-116 in instructing the outward translocation of lysosomes, this inhibition of lysosomal expulsion caused by the *unc-116* mutation resulted in the enlargement of a subset of lysosomes near the cell center (Fig. 6C), as indicated by larger lysosomes positioned farther from the plasma membrane in coelomocytes of *Is[nhx-2p::CPL-1::wrmScarlet]* worms (Fig. S6C). Notably, inhibiting the *unc-116* mutation-induced lysosome enlargement, by inhibiting lysosomal fusion via *cup-14(RNAi)* (Gee et al., 2017), only mildly recovered purgasome-mediated lysosome release (Fig. 6A), which supports that the decline in lysosome expulsion caused by the *unc-116* mutation is due to impaired lysosomal outward transport rather than lysosome enlargement. Moreover, lysosomes were evenly distributed in *Is[nhx-2p::CPL-1::wrmScarlet]* worms (Fig. 6B; S6D). In contrast, in *Is[nhx-2p::CPL-1::wrmScarlet]* worms carrying the *unc-116* mutation and subjected to *cup-14(RNAi)* to prevent lysosomal enlargement, lysosomes segregated into two distinct populations: one exhibiting higher substrate accumulation and the other showing lower substrate levels (Fig. 6D). Notably, lysosomes with higher substrate accumulation were positioned significantly farther from the plasma membrane than those with lower substrate levels (Fig. S6E), supporting that UNC-116 mediates selective outward transport of lysosomes with impaired degradative capacity.

Furthermore, increasing UNC-116 levels is sufficient to promote lysosomal expulsion, as evidenced by that overexpressing *unc-116* specifically in coelomocytes further increased purgasome-mediated lysosomal expulsion induced by CPL-1::wrmScarlet lysosomal overloading (Fig. 6E and F). Notably, consistent with the role of UNC-116 in outward translocating overloaded lysosomes (Fig. 6D; S6E), upon UNC-116 overexpression in coelomocytes, lysosomes exhibiting stronger CPL-1::wrmScarlet accumulation (Fig. 6F, red arrow) were located closer to the plasma membrane compared to those with weaker CPL-1::wrmScarlet signals (Fig. 6F, blue arrow; S6F), in contrast to the control group showing an even distribution (Fig. S6D). Therefore, UNC-116 preferentially drives the outward translocation of lysosomes with higher substrate accumulation.

382   Given the established role of RAB-7 in recruiting kinesin motors (Settembre and

383   Perera, 2023), and the requirement of both RAB-7 and UNC-116 for purgasome-

384   mediated lysosomal expulsion during lysosomal stress, we next examined their

385   potential interaction using a split-GFP assay (spGFP$_{11}$::RAB-7 and UNC-116::spGFP$_{1-}$

386   $_{10}$). In the absence of CPL-1::wrmScarlet lysosomal overloading, co-expression of

387   spGFP$_{11}$::RAB-7 and UNC-116::spGFP$_{1-10}$ in the coelomocytes produced undetectable

388   fluorescence (Fig. 6 G and I), reflecting negligible interaction between RAB-7 and

389   UNC-116 under homeostasis. Remarkably, upon CPL-1::wrmScarlet lysosomal

390   overloading, obvious split-GFP signals were detected on the lysosomes in

391   approximately 30% of coelomocytes at a specific time point (Fig. 6 H and I), as

392   indicated by the puncta displaying signals only in the GFP channel but not in the

393   wrmScarlet channel (Fig. 6 H, white arrow). The majority of these split-GFP signals

394   were localized to the lysosome periphery, as indicated by their proximity to the

395   lysosomal lumen, which was filled with CPL-1::wrmScarlet and exhibited spillover

396   signals in both the GFP and Scarlet channels (yellow arrow, Fig. 6H). These data

397   indicate increased interaction between RAB-7 and UNC-116 on the lysosomes under

398   lysosomal overload stress.

399   If the RAB-7-UNC-116 interaction is important for outward translocation of

400   lysosomes, downregulating RAB-7 should suppress the increase in purgasome-

401   mediated lysosomal export triggered by the elevation of UNC-116. Indeed, in *Is[nhx-*

402   *2p::CPL-1::wrmScarlet]* worms, *rab-7(RNAi)* suppressed the increase in lysosomal

403   export induced by *unc-116* overexpression (Fig. S6G). These genetic data further

404   support that RAB-7 and UNC-116 interact to direct lysosome expulsion. Collectively,

405   these findings demonstrate that lysosomal overload stress triggers the interaction

406   between RAB-7 and the kinesin motor UNC-116 on lysosomes, enabling their outward

407   translocation into purgasomes.

408   **Purgasome-mediated lysosomal expulsion preserves lysosomal degradative**

409   **function under stress**

410   Given that cytopurgosis preferentially expels overloaded lysosomes (Fig. 3A-D)

411   in a manner proportional to stress (Fig. 3E-G), we next tested its functional importance

412   in maintaining lysosomal homeostasis. We hypothesized that if cytopurgosis is a critical

413   quality control pathway, inhibiting it should worsen lysosomal substrate accumulation.

414   To test this, we blocked the pathway in *Is[nhx-2p::CPL-1::wrmScarlet]* worms in two

415   distinct ways: first, by disrupting outward transportation of lysosomes via *unc-116* loss-

416   of-function (Fig. 6 A-D), and second, by preventing purgasome budding through

417   coelomocyte-specific overexpression of ARF-6 (Fig. 4K). In both cases, inhibiting

418   cytopurgosis led to a significant increase in the accumulation of CPL-1::wrmScarlet

419   substrate within coelomocyte lysosomes (Fig. 6J and K). These results demonstrate that

420   inhibiting the expulsion of damaged lysosomes impairs the cell's ability to manage

421   lysosomal overload.

422   We then performed the reciprocal experiment to determine if enhancing

423   cytopurgosis could alleviate lysosomal storage. We stimulated the pathway either by

424   overexpressing the motor protein UNC-116 to enhance outward transport (Fig. 6 E and

425   F) or by using *arf-6(RNAi)* to promote purgasome formation (Fig. 4J) in *Is[nhx-*

426   *2p::CPL-1::wrmScarlet]* worms. Strikingly, both interventions significantly mitigated

427   the lysosomal accumulation of CPL-1::wrmScarlet in the coelomocytes (Fig. 6L and

428   M). Collectively, these complementary gain- and loss-of-function experiments

429   demonstrate that purgasome-mediated stressed lysosome expulsion is a fundamental

430   branch of the lysosomal quality control processes.

431   **DISCUSSION**

432   Cells have long been regarded as self-contained systems that eliminate unwanted

433   organelles through intracellular degradation via the autophagy-lysosome pathway. Here,

434   we define cytopurgosis, a previously unknown organelle-removal mechanism that

435   functions by expelling entire organelles into the extracellular space. We demonstrate

436   that cells package diverse organelles into large vesicles termed purgasomes, which form

437   through a plasma membrane budding process dependent on phosphatidylethanolamine

438   (PE) externalization (Fig. 6N). Critically, cytopurgosis functions as a biological "escape

439   valve," becoming markedly upregulated when the intracellular degradation machinery

440 is overwhelmed, such as during lysosomal overload or impaired autophagy. This

441 pathway is not a nonspecific disposal route; rather, it selectively targets and removes

442 overloaded lysosomes, thereby preserving lysosomal homeostasis (Fig. 6N). Thus,

443 purgasome-mediated organelle export serves as a fundamental mechanism for organelle

444 removal that complements intracellular degradation and is vital for maintaining cellular

445 homeostasis.

446 Our work distinguishes purgasomes from other known large EVs, establishing

447 them as a distinct entity. The identity of an EV is defined by its biogenesis, not its size.

448 Unlike exophers, whose formation mechanism remains unclear (Melentijevic et al.,

449 2017), purgasomes arise through plasma membrane budding driven by PE

450 externalization. Furthermore, purgasome biogenesis is mechanistically distinct from

451 migration-dependent vesicles like migrasomes and blebbisomes (Jeppesen et al., 2025;

452 Ma et al., 2014), highlighting its role as a universal, motility-independent disposal

453 pathway. The existence of multiple types of large EVs suggests that cells possess a

454 repertoire of specialized vesicular systems, each adapted to specific physiological

455 demands. For example, migrasomes may facilitate mitochondrial quality control in

456 motile cells, whereas cytopurgosis provides a motility-independent mechanism for

457 organelle disposal, particularly in response to an overwhelmed intracellular degradation

458 system. Future studies elucidating the regulation and functional specialization of these

459 vesicles will be crucial for understanding their individual roles.

460 Our discovery of purgasome-mediated lysosome expulsion reveals a new branch

461 of lysosomal quality control (LQC). Known LQC pathways primarily respond to

462 lysosomal membrane damage, employing ESCRT machinery or lipid transfer proteins

463 for repair, or triggering lysophagy to eliminate ruptured lysosomes (Yang and Tan,

464 2023). In contrast, cytopurgosis addresses functional impairment due to substrate

465 overload—a condition common in aging and lysosomal storage disorders (LSDs). The

466 marked upregulation of cytopurgosis in a Niemann-Pick type C1 (NPC1) model of

467 LSDs demonstrates its physiological relevance in chronic lysosomal pathology. This

468 finding opens a new avenue of investigation into whether lysosome expulsion mitigates

469   or contributes to disease progression in LSDs and other age-related conditions. A key

470   unresolved question is how cells balance and prioritize among these distinct LQC

471   pathways under varying stress conditions.

472   The identification of cytopurgosis redefines the landscape of organelle turnover in

473   cellular homeostasis. It establishes that organelle homeostasis is maintained through

474   two complementary systems: intracellular recycling via lysosomal degradation (Anding

475   and Baehrecke, 2017) and extracellular disposal via cytopurgosis. This extracellular

476   dimension introduces at least two novel concepts. First, cytopurgosis acts as a cellular

477   "escape valve," providing a compensatory clearance route when intracellular

478   degradation capacity is exceeded. Second, beyond its role in cellular cleansing,

479   purgasomes may serve as intercellular messengers, potentially eliciting systemic stress

480   responses in neighboring or distant cells, a possibility that warrants further investigation.

481   An important question will be to understand the interplay between these intracellular

482   and extracellular disposal systems. In conclusion, our discovery of cytopurgosis where

483   cells actively eject diverse organelles to survive stress broadens the paradigm of cellular

484   homeostasis maintenance and opens up a new field of investigation into the

485   extracellular fate of organelles.

486   **Materials and Methods**

487   **Worm strains and maintenance**

488   The strains used in this study are as follows: N2, XW11282 *qxIs520 [vha-*

489   *6p::LAAT-1::GFP]*, NP871 *unc-119(ed3) III; cdIs66 [cc1p::GFP::rab-7 + myo-*

490   *2p::GFP + unc-119(+)]*, RT258 *unc-119(ed3) III; pwIs50 [LMP-1::GFP + Cbr-unc-*

491   *119(+)]*, NP898 *cdIs80 [cc1p::PH::GFP, rol-6(su1006)]*, JT10800 *ncr-2(nr2023)*

492   *III; ncr-1(nr2022) X,* NP1360 *arIs37 [myo-3p::ssGFP + dpy-20(+)] I; cup-14(cd31),*

493   FF41 *unc-116(e2310) III,* CZ30889 *Is[pad-1(ju1806) + mec-4p::GFP(zdIs5)]; sax-*

494   *2(ju1815)*, MAT401 *jefIs41 [nhx-2p::CPL-1::wrmScarlet] (line#1)*, MAT402 *jefIs42*

495   *[nhx-2p::CPL-1::wrmScarlet] (line#2),* MAT403 *jefIs43 [nhx-2p::SP::wrmScarlet]*,

496   MAT404 *jefIs44 [unc-122p::LMP-1::GFP],* MAT405 *jefIs45 [unc-122p::GFP::MCA-*

497   *3-],*   MAT406   jefIs46[*unc-122p::GFP::GAL3*],   PHX10356   *sybIs10356[unc-*

498   *122p::PPK-1::GFP],*   MAT407   *jefIs50[unc-122p::UNC-116::GFP],*   MAT408

499   *jefIs51[unc-122p::GFP$_{11}$::RAB-7+unc-122p::UNC-116::GFP$_{1-10}$],*   MAT409

500   *jefIs53[unc-122P::ARF-6::GFP],*   MAT410   *jefIs44[unc-122p::LMP-1::GFP];*

501   *jefIs41[nhx-2p::CPL-1::wrmScarlet]*   *(line#1),*   MAT411   *jefIs45[unc-*

502   *122p::GFP::MCA-3]; jefIs41[nhx-2p::CPL-1::wrmScarlet]*   *(line#1),*   MAT412

503   *qxIs520[vha-6p::LAAT-1::GFP]; jefIs41[nhx-2p::CPL-1::wrmScarlet]*   *(line#1),*

504   MAT413   *jefIs46[unc-122p::GFP::GAL3]; jefIs41[nhx-2P::CPL-1::wrmScarlet]*

505   *(line#1),*   MAT414   *ncr-1(nr2022);jefIs41[nhx-2p::CPL-1::wrmScarlet]*   *(line#1),*

506   MAT415 *cdIs80[cc1p::PH::GFP, rol-6(su1006)]; jefIs41[nhx-2p::CPL-1::wrmScarlet]*

507   *(line#1),*   MAT416   *jefIs41[nhx-2p::CPL-1::wrmScarlet]*   *(line#1); pwIs170[vha-*

508   *6p::GFP::rab-7 + Cbr-unc-119(+)],* MAT417 *jefIs41[nhx-2p::CPL-1::wrmScarlet]*

509   *(line#1);pwIs170[vha-6p::GFP::rab-7 + Cbr-unc-119(+)]/+,*   MAT418   *unc-*

510   *116(e2310); jefIs41[nhx-2p::CPL-1::wrmScarlet]*   *(line#1),* MAT419 *jefIs50[unc-*

511   *122p::UNC-116::GFP]; jefIs41[nhx-2p::CPL-1::wrmScarlet]*   *(line#1),*   MAT420

512   *jefIs52[unc-122p::ARF-6::GFP]; jefIs41[nhx-2p::CPL-1::wrmScarlet]*   *(line#1),*

513   MAT421   *jefIs44[unc-122p::LMP-1::GFP]; jefIs43[nhx-2p::SP::wrmScarlet],*

514   MAT422   *jefIs45[unc-122p::GFP::MCA-3]; jefIs43[nhx-2p::SP::wrmScarlet],*

515   MAT423   *jefIs51[unc-122p::GFP$_{11}$::RAB-7+unc-122p::UNC-116::GFP$_{1-10}$];*

516   *jefIs41[nhx-2p::CPL-1::wrmScarlet]*   *(line#1)* and MAT424   *sybIs10356[unc-*

517   *122p::PPK-1::GFP]; jefIs41[nhx-2p::CPL-1::wrmScarlet]*   *(line#1),*   MAT429

518   *jefIs54[nhx-2p::CPL-1 (C144A)::wrmScarlet],* MAT430 *pad-1(ju1806); jefIs41[nhx-*

519   *2p::CPL-1::wrmScarlet] (line#1).* All *C. elegans* strains were grown on NGM medium

520   spotted with OP50 *E. coli* bacteria and maintained at 20°C unless otherwise indicated.

521   **Plasmid construction and generation of transgenic strains**

522   All *C. elegans* genetic sequences were amplified from N2 strain genomic DNA

523   (gDNA) or cDNA. The human Galectin-3 sequence was amplified from HeLa cell

524   cDNA. For tissue-specific expression, the intestine-specific *nhx-2* promoter and the

525   coelomocyte-specific *unc-122* promoter, each approximately 1.9 kb upstream of their

526   respective coding sequences, were amplified from N2 gDNA. The *nhx-2* promoter was

527   subsequently cloned into the pBSK vector using KpnI and HindIII restriction sites,

528   while the *unc-122* promoter was cloned into the HT76 vector using AvrII and BamHI

529   sites. Genomic sequences for *cpl-1*, *lmp-1*, *arf-6*, and *rab-7*, and cDNA sequences for

530   the *sel-1* signal peptide, *unc-116*, *mca-3*, and *ppk-1* were then cloned into these

531   expression backbones as required. All final constructs were verified by Sanger

532   sequencing.

533   Transgenic *C. elegans* strains were generated by standard microinjection of DNA

534   constructs into the N2 germline to create lines carrying extra-chromosomal arrays. To

535   generate stable, integrated lines, these arrays were subjected to X-ray irradiation using

536   an RS2000 pro X-ray irradiator (Rad Source). The resulting integrated lines were

537   outcrossed before use in experiments.

Purgasome quantification and imaging

539   For high-throughput quantification of purgasome numbers, a Nikon SMZ18

540   stereomicroscope was utilized. Stage-synchronized day-3 adult hermaphrodites

541   carrying the transgenes *jefIs41[nhx-2p::CPL-1::wrmScarlet]* (line #1), *jefIs42[nhx-*

542   *2p::CPL-1::wrmScarlet]* (line #2), or *jefIs43 [nhx-2p::SP::wrmScarlet]* were scored.

543   Purgasomes were identified as distinct extracellular vesicles containing wrmScarlet-

544   positive puncta, and the total number produced by all six coelomocytes was manually

545   counted for each animal.

546   For detailed morphological analysis and quantification, worms were imaged on a

547   Zeiss LSM 900 confocal microscope equipped with a 63× oil-immersion objective.

548   Day-3 adult animals expressing either *pwIs50 [LMP-1::GFP]* or *jefIs41 [nhx-2p::CPL-*

549   *1::wrmScarlet]* (line #1) transgene were immobilized on 3% agarose pads with 10 mM

550   levamisole. Differential interference contrast (DIC) was used to visualize purgasome

551   morphology. Lysosome-containing purgasomes were identified by detecting either

552   LMP-1::GFP (488 nm excitation) or CPL-1::wrmScarlet (561 nm excitation), and the

553   total number from all coelomocytes was quantified per animal.

RNA interference (RNAi)

555   RNAi was performed by the standard feeding method using bacterial strains from

556 the ORF-RNAi (GE Dharmacon) and MRC (Source BioScience) libraries. Bacteria

557 expressing dsRNA targeting the gene of interest were cultured and seeded onto

558 nematode growth medium (NGM) plates supplemented with 1 mM IPTG and 25 μg/mL

559 ampicillin. For most experiments, synchronized L1 larvae were placed on the RNAi

560 plates to develop. In cases where knockdown caused larval lethality or severe

561 developmental defects, RNAi was initiated at the L4 stage to allow animals to reach

562 adulthood for analysis. Worms were transferred to fresh RNAi plates as required to

563 prevent starvation. All phenotypes, including purgasome quantification, were scored on

564 day 3 of adulthood in the P0 generation. Bacteria transformed with the L4440 empty

565 vector were used as the negative control in all experiments.

566 **Microscopic analyses of lysosomal substrate**

567 High-resolution fluorescence analysis of lysosomal substrates was performed on a

568 Zeiss LSM 900 confocal microscope with a 63× oil-immersion objective. Worms of the

569 specified genotypes and treatments were immobilized on 3% agarose pads with 10 mM

570 levamisole. This setup was used to image wrmScarlet-tagged substrates (CPL-

571 1::wrmScarlet, sp::wrmScarlet, CPL-1(C144A)::wrmScarlet) within coelomocytes,

572 purgasomes, and the intestine.

573 For whole-animal fluorescence overview and quantification, a wide-field Nikon

574 DS-Qi2 upright microscope with a 20× air objective was used. Animals were similarly

575 immobilized with 10 mM levamisole. The fluorescence of all acquired images from

576 both microscope systems were quantified using either ImageJ or Imaris 10.

577 **Imaging and quantification of lysosomal localization of CPL-1::wrmScarlet in**

578 **coelomocytes**

579 To evaluate the lysosomal localization of CPL-1::wrmScarlet in coelomocytes, we

580 utilized the MAT410 strain (*jefIs44 [unc-122p::LMP-1::GFP]; jefIs41 [nhx-2p::CPL-*

581 *1::wrmScarlet]*, (line #1). For analysis, coelomocytes were randomly selected and

582 imaged using a Zeiss LSM 900 confocal microscope with a 63× oil immersion objective.

583 Fluorescence signals for GFP and wrmScarlet were captured by excitation at 488 nm

584 and 561 nm, respectively, using Airyscan mode to enhance resolution. Z-stacks were

585 systematically acquired by adjusting the focal plane along the Z-axis and subsequently

586 processed in Imaris 10 software. For quantification, 10 coelomocytes were randomly

587 selected in each experiment. Three independent biological replicates were performed

588 for each strain and quantified accordingly.

589 Imaging and quantification of lysosomal localization of CPL-1::wrmScarlet in

590 intestinal cells

591 Intestinal cells from worms expressing the transgene *Is[nhx-2p::CPL-*

592 *1::wrmScarlet]* along with the lysosomal marker LAAT-1::GFP were randomly selected

593 for imaging. Confocal microscopy was performed using a Zeiss LSM 900 microscope

594 equipped with a 63× oil immersion objective and Airyscan detection to achieve

595 enhanced resolution. GFP and wrmScarlet fluorescence were excited at 488 nm and 561

596 nm, respectively. Images were acquired and analyzed using Imaris 10 software, which

597 automatically detected red fluorescent signal (CPL-1::wrmScarlet) surrounded by

598 LAAT-1::GFP-labeled lysosomes and quantified the corresponding wrmScarlet

599 fluorescence intensity.

600 Imaging and quantification of lysosomal CPL-1::wrmScarlet in coelomocytes and

601 purgasomes

602 Lysosomal CPL-1::wrmScarlet in coelomocytes and purgasomes was visualized

603 using a Zeiss LSM 900 confocal microscope equipped with a 63× oil immersion

604 objective. Differential interference contrast (DIC) microscopy was used to delineate the

605 boundaries of coelomocytes and purgasome membranes, while fluorescence from CPL-

606 1::wrmScarlet was excited with a 561-nm laser. Mean fluorescence intensity of

607 lysosomal CPL-1::wrmScarlet in both cell types was quantified using ImageJ. For each

608 experimental replicate, 20 coelomocytes and their associated purgasomes were

609 randomly selected and analyzed per strain. Analyses were performed across three

610 independent biological replicates for each strain.

611 Quantification of plasma membrane fluorescence

612 To quantify fluorescence at the coelomocyte plasma membrane, worms expressing

613 either PH::GFP or PPK-1::GFP were imaged on a Zeiss LSM 900 confocal microscope.

614   The resulting images were analyzed using Imaris 10 software. For each coelomocyte,

615   four regions of interest (ROIs) of a similar size were randomly selected along the

616   plasma membrane. The mean fluorescence intensity within these ROIs was measured,

617   and the average of the four values was calculated to represent the fluorescence intensity

618   for that cell. This analysis was conducted on a total of 60 coelomocytes per strain,

619   collected from three independent biological replicates (n=20 cells per replicate).

620   **Quantification of coelomocyte, purgasome, and lysosome size**

621   To measure the size of coelomocytes and purgasomes, images were acquired on a

622   Nikon DS-Qi2 wide-field microscope equipped with a 40× oil-immersion objective.

623   Both differential interference contrast (DIC) and Texas Red (TxRed) fluorescence

624   channels were used to visualize overall morphology and internal wrmScarlet-labeled

625   lysosomes, respectively. The maximum diameter of individual coelomocytes and

626   purgasomes was measured from these images using ImageJ. For the analysis of

627   lysosome size, a relative classification was performed within each cell. The mean

628   diameter of all visible lysosomes was calculated for a given coelomocyte, establishing

629   a cell-specific threshold. Individual lysosomes were then classified as 'large' if their

630   diameter was above this mean and 'small' if their diameter was below it.

631   **Analysis of lysosome distance from the plasma membrane**

632   The spatial distribution of lysosomes within coelomocytes was quantified by

633   measuring their distance from the plasma membrane. Worms with CPL-1::wrmScarlet-

634   filled lysosomes were imaged on a Zeiss LSM 900 confocal microscope using a 63×

635   oil-immersion objective. Z-stack images were acquired using both differential

636   interference contrast (DIC) to define the cell boundary and a 561 nm laser to visualize

637   the lysosomes. Using ImageJ, the shortest distance from the geometric center of each

638   individual lysosome to the nearest point on the coelomocyte plasma membrane was

639   measured in the central focal plane of the cell.

640   **Quantification of lysosomal substrate in forming purgasomes**

641   To compare the properties of lysosomes within budding purgasomes to their

intracellular counterparts, approximately 10,000 day-3 adult *jefIs41 [nhx-2p::CPL-1::wrmScarlet]* worms were screened on a Zeiss LSM 900 confocal microscope with a 63× oil-immersion objective to identify the rare event of a coelomocyte actively forming a purgasome. On average, around 1,000 worms were examined to detect a single forming purgasome. Upon successful identification, high-resolution images were captured using differential interference contrast (DIC) to visualize morphology and a 561 nm laser to detect CPL-1::wrmScarlet-labeled lysosomes. Using ImageJ, the mean fluorescence intensity and diameter of individual lysosomes were measured for two populations within the same cell: (1) lysosomes located within the budding purgasome and (2) lysosomes remaining in the intracellular space. Lysosome diameter was measured as described previously.

Transmission Electron Microscopy (TEM)

Day-3 adult *jefIs41[nhx-2p::CPL-1::wrmScarlet]* worms were prepared for TEM analysis by high-pressure freezing and freeze substitution (HPF/FS), following an established protocol (Liu et al., 2023). Briefly, worms were transferred into M9 buffer with 20% BSA and high-pressure frozen in a Leica EM ICE. Freeze substitution was conducted in a Leica EM AFS2 system over six days using an acetone solution containing 1% osmium tetroxide, 0.1% uranyl acetate, and 10% methanol. The temperature was gradually raised to 20°C, and samples were rinsed with pure acetone.

For embedding, samples were infiltrated with Epon resin using a graded series of acetone:Epon mixtures (1:3, 1:2, 1:1, and 3:1) for 3 hours each, followed by four 6-hour incubations in 100% Epon resin on a rotator. Samples were first flat-embedded between ACLAR films and polymerized at 60°C for 24 hours. Regions containing coelomocytes and purgasomes were then excised, re-embedded in fresh resin within molds, and polymerized for an additional 48 hours at 60°C.

Serial ultrathin sections (~70 nm) were cut on a Leica EM UC7 ultramicrotome and collected onto copper grids. For correlative analysis, adjacent sections were stained with 1% toluidine blue to identify the locations of coelomocytes and purgasomes under a light microscope. Ultrathin sections were then imaged at 80 kV on a Thermo Fisher

671 Scientific Talos L120C TEM equipped with a 4k × 4k Ceta camera. Images were

672 acquired using Velox software (v2.8.0.898).

Correlative Light and Electron Microscopy (CLEM)

674 To correlate fluorescently labeled structures with their ultrastructure, day-3 adult

675 *jefIs41[nhx-2p::CPL-1::wrmScarlet]* worms were processed for embedding as

676 described for TEM. From the resin blocks, serial sections were prepared. First, a 400

677 nm-thick section was collected and imaged on a Zeiss LSM 900 confocal microscope.

678 Fluorescence images were acquired using a 561 nm laser to identify the positions of

679 CPL-1::wrmScarlet-labeled coelomocytes and purgasomes. Immediately following this,

680 an adjacent 70 nm-thick ultrathin section was collected from the same region of the

681 block and imaged via TEM as described above to obtain high-resolution ultrastructural

682 data. The resulting fluorescence (light microscopy) and ultrastructural (electron

683 microscopy) images were then aligned using non-rigid registration in the Icy software

684 with the ec-CLEMv2 plugin to generate the final correlated images.

Split-GFP complementation assay for RAB-7 and UNC-116 interaction

686 The interaction between RAB-7 and UNC-116 was assessed in vivo using a split-

687 GFP complementation assay. A strain co-expressing *jefIs51[unc-122p::spGFP$_{11}$::RAB-*

688 *7 + unc-122p::UNC-116::spGFP$_{1-10}$]* in coelomocytes was generated (MAT408). This

689 strain was crossed with *jefIs41 [nhx-2p::CPL-1::wrmScarlet]* to create a lysosomal

690 overload condition (MAT423). Coelomocytes from both strains were imaged on a Zeiss

691 LSM 900 confocal microscope. A positive interaction event was defined by the

692 reconstitution of a functional GFP fluorophore, appearing as a distinct GFP signal (488

693 nm excitation). The scoring criteria were highly specific: a true split-GFP signal was

694 counted only if it appeared as a punctum labeling the lysosome periphery and did not

695 co-localize with the wrmScarlet signal (561 nm excitation). This allowed genuine GFP

696 reconstitution to be distinguished from the spectral spillover of the bright CPL-

697 1::wrmScarlet signal from the lysosomal lumen, which appears in both green and red

698 channels. Coelomocytes displaying one or more such specific GFP puncta were scored

699 as positive for interaction.

Investigation of potential membranous thin fibers between coelomocytes and purgasomes

To determine if purgasome formation involves plasma membrane-derived thin fibers, similar to those reported for other large EVs, we used a dual-labeled strain *jefIs41[nhx-2p::CPL-1::wrmScarlet]; jefIs45[unc-122p::GFP::MCA-3]* expressing a wrmScarlet-tagged lysosomal marker and a GFP-tagged plasma membrane marker (GFP::MCA-3). Animals were imaged on a Zeiss LSM 900 confocal microscope with a 63× oil objective. Complete Z-stacks were acquired to capture the entire volume between a coelomocyte and any adjacent purgasomes. Each Z-stack was then systematically inspected for any continuous, GFP::MCA-3-positive structures, such as thin fibers or nanotubes, that would indicate a physical connection between the two bodies.

Quantification of lysosomal substrate in peripheral and central regions of coelomocytes

To analyze the spatial distribution of lysosomes, coelomocytes from worms of the indicated genotypes were imaged on a Zeiss LSM 900 confocal microscope. For each cell, the image was computationally divided into two compartments for analysis. First, the cell was modeled as an ellipse, and a concentric inner ellipse was drawn at 50% of the radial distance from the geometric center to the plasma membrane. This divided the cell into an inner "central region" and an outer "peripheral region" of equal radial thickness. The mean fluorescence intensity of CPL-1::wrmScarlet-labeled lysosomes within each of these two regions was then quantified using ImageJ. In the UNC-116 overexpression group, only coelomocytes displaying reduced lysosomal size, a feature of UNC-116 overexpression, were included in the analysis.

Detection of Phosphatidylethanolamine (PE) externalization

To detect externalized PE, coelomocytes and purgasomes were released from day-3 adult worms of the indicated genotypes and treatments. Approximately 200 animals were dissected in 200 μL of imaging medium (L-15 medium [Gibco, 21083-027]

728 supplemented with 15% fetal bovine serum [Gibco, 10270-106] and 1% sucrose [Sigma,

729 57-50-1]). PE was labeled by adding 100 nM biotinylated Duramycin (MTTI, D-1003)

730 and 1.5 mg/mL Alexa Fluor 488-conjugated streptavidin (AAT Bioquest, 16891) to the

731 medium. The cell suspension was immediately transferred to a 20 mm glass-bottom

732 dish (NEST, 80100) and imaged on a Nikon Eclipse Ti2 inverted microscope with a

733 40× oil-immersion objective. The fluorescence intensity of the Duramycin signal on the

734 surface of coelomocytes and purgasomes was quantified using Imaris 10. For each

735 biological replicate, 20 coelomocytes and 10 purgasomes were randomly selected for

736 analysis.

Statistical analysis

738 All statistical analyses were performed using GraphPad Prism v9. Data are

739 presented as mean ± standard error of the mean (S.E.M.). Specific statistical tests were

740 chosen based on the experimental design. For comparisons of multiple groups to a

741 single control, a one-way ANOVA followed by Dunnett's multiple comparisons test

742 was used. For pairwise comparisons among all groups in a multi-group experiment, a

743 one-way ANOVA with Tukey's multiple comparisons test was applied. All other

744 comparisons between two independent groups were analyzed using an unpaired, two-

745 tailed Student's t-test. A P-value < 0.05 was considered statistically significant (*p $<$

746 0.05, **p < 0.01, ***p < 0.001, ****p < 0.0001). To prevent bias, sample information

747 was blinded prior to analysis, and worms and cells were randomly selected for imaging.

748

764 **AUTHOR CONTRIBUTIONS**

765   H.T. supervised the entire study. H.T. and L.W. conceived the research. L.W. and

766 Y.L. designed and performed the experiments and analyzed the data. H.T, L.W., and

767 Y.L. wrote the manuscript, with input from all authors.

768 **DECLARATION OF INTERESTS**

769   The authors declare the following competing interests: All authors are inventors

770 on a patent application (Application No. CN2025119599427) related to this work.

771 **REFERENCES**

772 Anding, A.L. and Baehrecke, E.H. (2017). Cleaning House: Selective Autophagy of

773 Organelles. Developmental Cell *41*, 10-22.

774 Bednarek, E.M., Schaheen, L., Gaubatz, J., Jorgensen, E.M. and Fares, H. (2007). The

775 Plasma Membrane Calcium ATPase MCA‑3 is Required for Clathrin‑Mediated

776 Endocytosis in Scavenger Cells of Caenorhabditis elegans. Traffic *8*, 543-553.

777 Beer, K.B., Rivas-Castillo, J., Kuhn, K., Fazeli, G., Karmann, B., Nance, J.F., Stigloher,

778 C. and Wehman, A.M. (2018). Extracellular vesicle budding is inhibited by redundant

779 regulators of TAT-5 flippase localization and phospholipid asymmetry. Proceedings of

780 the National Academy of Sciences *115*, E1127–E1136.

781 Brown, F.D., Rozelle, A.L., Yin, H.L., Balla, T.s. and Donaldson, J.G. (2001).

782 Phosphatidylinositol 4,5-bisphosphate and Arf6-regulated membrane traffic. The

783 Journal of Cell Biology *154*, 1007-1018.

784 Cabukusta, B. and Neefjes, J. (2018). Mechanisms of lysosomal positioning and

785   movement. Traffic *19*, 761-769.

786   Eguchi, T., Kuwahara, T., Sakurai, M., Komori, T., Fujimoto, T., Ito, G., Yoshimura, S.-

787   i., Harada, A., Fukuda, M., Koike, M. and Iwatsubo, T. (2018). LRRK2 and its substrate

788   Rab GTPases are sequentially targeted onto stressed lysosomes and maintain their

789   homeostasis. Proceedings of the National Academy of Sciences *115*, E9115–E9124.

790   Gee, K., Zamora, D., Horm, T., George, L., Upchurch, C., Randall, J., Weaver, C.,

791   Sanford, C., Miller, A., Hernandez, S., et al. (2017). Regulators of Lysosome Function

792   and Dynamics in Caenorhabditis elegans. G3 Genes|Genomes|Genetics *7*, 991-1000.

793   Hu, H., Sa, Q., Koehler, T.M., Aronson, A.I. and Zhou, D. (2006). Inactivation of

794   Bacillus anthracis spores in murine primary macrophages. Cellular Microbiology *8*,

795   1634-1642.

796   Hung, Y.-H., Chen, L.M.-W., Yang, J.-Y. and Yuan Yang, W. (2013). Spatiotemporally

797   controlled induction of autophagy-mediated lysosome turnover. Nature

798   Communications *4*

799   Jeppesen, D.K., Sanchez, Z.C., Kelley, N.M., Hayes, J.B., Ambroise, J., Koory, E.N.,

800   Krystofiak, E., Taneja, N., Zhang, Q., Dungan, M.M., et al. (2025). Blebbisomes are

801   large, organelle-rich extracellular vesicles with cell-like properties. Nature Cell Biology

802   *27*, 438-448.

803   Jia, J., Claude-Taupin, A., Gu, Y., Choi, S.W., Peters, R., Bissa, B., Mudd, M.H., Allers,

804   L., Pallikkuth, S., Lidke, K.A., et al. (2020). Galectin-3 Coordinates a Cellular System

805   for Lysosomal Repair and Removal. Developmental Cell *52*, 69-87 e68.

806   Jiao, H., Jiang, D., Hu, X., Du, W., Ji, L., Yang, Y., Li, X., Sho, T., Wang, X., Li, Y., et

807   al. (2021). Mitocytosis, a migrasome-mediated mitochondrial quality-control process.

808   Cell *184*, 2896-2910 e2813.

809   Khaminets, A., Heinrich, T., Mari, M., Grumati, P., Huebner, A.K., Akutsu, M.,

810   Liebmann, L., Stolz, A., Nietzsche, S., Koch, N., et al. (2015). Regulation of

811   endoplasmic reticulum turnover by selective autophagy. Nature *522*, 354-358.

812   Kurihara, Y., Kanki, T., Aoki, Y., Hirota, Y., Saigusa, T., Uchiumi, T. and Kang, D.

813   (2012). Mitophagy Plays an Essential Role in Reducing Mitochondrial Production of

814   Reactive Oxygen Species and Mutation of Mitochondrial DNA by Maintaining

815   Mitochondrial Quantity and Quality in Yeast. Journal of Biological Chemistry *287*,

816   3265-3272.

817   Li, W., He, P., Huang, Y., Li, Y.-F., Lu, J., Li, M., Kurihara, H., Luo, Z., Meng, T., Onishi,

818   M., et al. (2021). Selective autophagy of intracellular organelles: Recent research

819   advances. Theranostics *11*, 222-256.

820   Lim, C.-Y., Davis, O.B., Shin, H.R., Zhang, J., Berdan, C.A., Jiang, X., Counihan, J.L.,

821   Ory, D.S., Nomura, D.K. and Zoncu, R. (2019). ER – lysosome contacts enable

822   cholesterol sensing by mTORC1 and drive aberrant growth signalling in Niemann–Pick

823   type C. Nature Cell Biology *21*, 1206-1218.

824   Liu, P., Shi, J., Sheng, D., Lu, W., Guo, J., Gao, L., Wang, X., Wu, S., Feng, Y., Dong,

825   D., et al. (2023). Mitopherogenesis, a form of mitochondria-specific ectocytosis,

826   regulates sperm mitochondrial quantity and fertility. Nature Cell Biology *25*, 1625-

827   1636.

828   Ma, L., Li, Y., Peng, J., Wu, D., Zhao, X., Cui, Y., Chen, L., Yan, X., Du, Y. and Yu, L.

829   (2014). Discovery of the migrasome, an organelle mediating release of cytoplasmic

830   contents during cell migration. Cell Research *25*, 24-38.

831   Maejima, I., Takahashi, A., Omori, H., Kimura, T., Takabatake, Y., Saitoh, T.,

832   Yamamoto, A., Hamasaki, M., Noda, T., Isaka, Y. and Yoshimori, T. (2013). Autophagy

833   sequesters damaged lysosomes to control lysosomal biogenesis and kidney injury. The

834   EMBO Journal *32*, 2336-2347.

835   Melentijevic, I., Toth, M.L., Arnold, M.L., Guasp, R.J., Harinath, G., Nguyen, K.C.,

836   Taub, D., Parker, J.A., Neri, C., Gabel, C.V., et al. (2017). *C. elegans* neurons jettison

837   protein aggregates and mitochondria under neurotoxic stress. Nature *542*, 367-371.

838   Nehrke, K. and Melvin, J.E. (2002). The NHX Family of Na^+-H^+ Exchangers in

839   Caenorhabditis elegans. Journal of Biological Chemistry *277*, 29036-29044.

840   Park, S., Noblett, N., Pitts, L., Colavita, A., Wehman, A.M., Jin, Y. and Chisholm, A.D.

841   (2024). Dopey-dependent regulation of extracellular vesicles maintains neuronal

842   morphology. Current Biology *34*, 4920-4933 e4911.

843   Platt, F.M., d'Azzo, A., Davidson, B.L., Neufeld, E.F. and Tifft, C.J. (2018). Lysosomal

844   storage diseases. Nature Reviews Disease Primers *4*

845   Radulovic, M., Schink, K.O., Wenzel, E.M., Nähse, V., Bongiovanni, A., Lafont, F. and

846   Stenmark, H. (2018). ESCRT‐mediated lysosome repair precedes lysophagy and

847   promotes cell survival. The EMBO Journal *37*, e99753.

848   Sandoval, H., Thiagarajan, P., Dasgupta, S.K., Schumacher, A., Prchal, J.T., Chen, M.

849   and Wang, J. (2008). Essential role for Nix in autophagic maturation of erythroid cells.

850   Nature *454*, 232-235.

851   Settembre, C. and Perera, R.M. (2023). Lysosomes as coordinators of cellular

852   catabolism, metabolic signalling and organ physiology. Nature Reviews Molecular Cell

853   Biology *25*, 223-245.

854   Sica, V., Galluzzi, L., Bravo-San Pedro, José M., Izzo, V., Maiuri, Maria C. and

855   Kroemer, G. (2015). Organelle-Specific Initiation of Autophagy. Molecular Cell *59*,

856   522-539.

857   Skowyra, M.L., Schlesinger, P.H., Naismith, T.V. and Hanson, P.I. (2018). Triggered

858   recruitment of ESCRT machinery promotes endolysosomal repair. Science *360*,

859   eaar5078.

860   Stenmark, H. (2009). Rab GTPases as coordinators of vesicle traffic. Nature Reviews

861   Molecular Cell Biology *10*, 513-525.

862   Sun, Y., Cao, Y., Wan, H., Memetimin, A., Cao, Y., Li, L., Wu, C., Wang, M., Chen, S.,

863   Li, Q., et al. (2024). A mitophagy sensor PPTC7 controls BNIP3 and NIX degradation

864   to regulate mitochondrial mass. Molecular Cell *84*, 327-344 e329.

865   Tan, J.X. and Finkel, T. (2022). A phosphoinositide signalling pathway mediates rapid

866   lysosomal repair. Nature *609*, 815-821.

867   Tang, L., Fares, H., Zhao, X., Du, W. and Liu, B.-F. (2012). Different endocytic

868   functions of AGEF-1 in C. elegans coelomocytes. Biochimica et Biophysica Acta (BBA)

869   - General Subjects *1820*, 829-840.

870   Turek, M., Banasiak, K., Piechota, M., Shanmugam, N., Macias, M., Sliwinska, M.A.,

871   Niklewicz, M., Kowalski, K., Nowak, N., Chacinska, A. and Pokrzywa, W. (2021).

872 Muscle-derived exophers promote reproductive fitness. EMBO Rep *22*, e52071.

873 Wehman, A.M., Poggioli, C., Schweinsberg, P., Grant, B.D. and Nance, J. (2011). The

874 P4-ATPase TAT-5 inhibits the budding of extracellular vesicles in *C. elegans* embryos.

875 Curr Biol *21*, 1951-1959.

876 Xu, M., Liu, Y., Zhao, L., Gan, Q., Wang, X., Yang, C. and Spang, A. (2014). The

877 lysosomal cathepsin protease CPL-1 plays a leading role in phagosomal degradation of

878 apoptotic cells in *Caenorhabditis elegans*. Molecular Biology of the Cell *25*, 2071-2083.

879 Yang, H. and Tan, J.X. (2023). Lysosomal quality control: molecular mechanisms and

880 therapeutic implications. Trends in Cell Biology *33*, 749-764.

881 Youle, R.J. and Narendra, D.P. (2010). Mechanisms of mitophagy. Nature Reviews

882 Molecular Cell Biology *12*, 9-14.

883

884

885

886

887

888

889

890

891

892

893

894

895

896

897
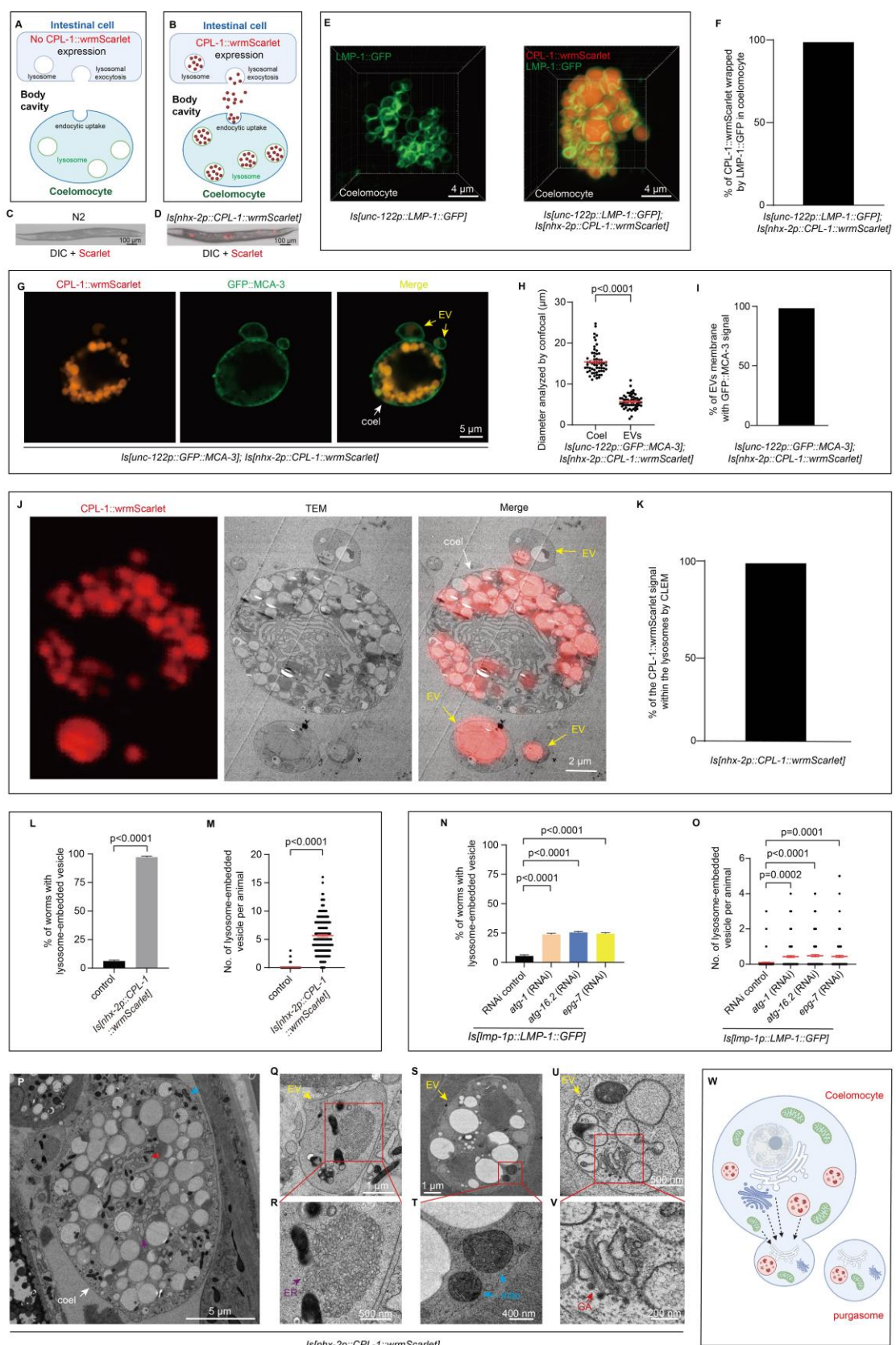
898

899

900

Figure 1: Purgasomes are generated to expel various organelles, which is enhanced when the intracellular clearance capacity is compromised

A-D, Schematic illustrations and images depicting CPL-1::wrmScarlet release via lysosomal exocytosis from the intestinal cells, followed by endocytic uptake and lysosomal accumulation in coelomocytes. Microscopic analysis reveals the accumulation of CPL-1::wrmScarlet in coelomocytes (D), which originates from intestinal secretion via lysosomal exocytosis in the transgenic line *Is[nhx-2p::CPL-1::wrmScarlet]* (D), corresponding to panel B. The N2 wild-type worms (C) serve as the control, corresponding to panel A. The *nhx-2* promoter directs gene expression specifically in intestinal cells of the worms.

E-F, Volumetric rendering images and a bar graph show the accumulation of CPL-1::wrmScarlet in lysosomes of coelomocytes from the transgenic strain *Is[nhx-2p::CPL-1::wrmScarlet]* (E, right), in contrast to the control strain that lacks CPL-1::wrmScarlet expression (E, left). The lysosomal membrane was labeled with LMP-1::GFP, specifically expressed in coelomocytes under the control of the *unc-122* promoter. CPL-1::wrmScarlet fluorescence encapsulated within lysosomes surrounded by LMP-1::GFP was quantified in (F). n=30 coelomocytes (F).

G-I, Fluorescence micrograph, bar graph and scatter plot depicting lysosome-embedded extracellular vesicles (EVs) produced by the coelomocytes (coel), as evidenced by the origin of EV membranes from the coelomocyte plasma membrane. Green, GFP::MCA-3 (plasma membrane); red, CPL-1::wrmScarlet (lysosomes) in (G). Diameter of coelomocytes and lysosome-embedded extracellular vesicles were quantified in (H). The membranes of EVs were uniformly labeled with the plasma membrane marker GFP::MCA-3, as shown in (I). Each dot represents the diameter of individual coelomocyte or lysosome-embedded EV (H). n=60 coelomocytes and 60 EVs (H); n=60 EVs (I). Two-tailed unpaired t tests were used for statistical analyses (H).

J and K, Representative correlative light-electron micrograph and bar graphs depicting the localization of CPL-1::wrmScarlet within the lysosome of the coelomocyte (coel)

930   and adjacent EVs in the *Is[nhx-2p::CPL-1::wrmScarlet]* strain. Quantitative analysis

931   reveals that all CPL-1::wrmScarlet signal is confined to the lysosomal lumen (K). n =

932   17 lysosomes from 11 EVs (K).

933   **L and M,** Graphs showing the percentage of worms generating lysosome-embedded

934   EVs (L) and the number of lysosome-embedded EVs per animal (M) in the *Is[nhx-*

935   *2p::CPL-1::wrmScarlet]* strain. Each dot represents the number of EVs per worm (M).

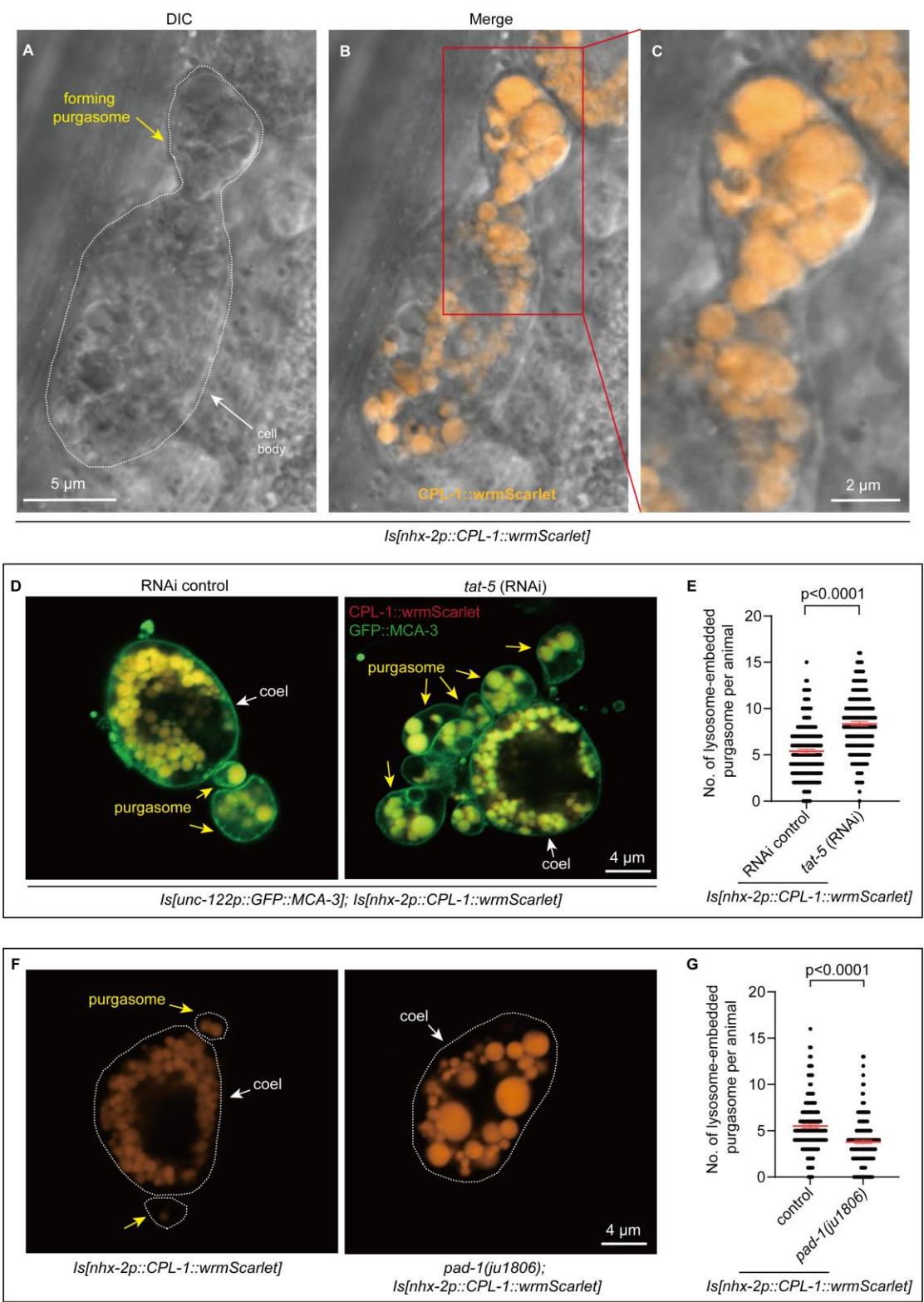936   n=180 animals (L and M). Two-tailed unpaired t tests were used for statistical analyses.

937   **N and O,** Graphs show the low percentage of worms containing lysosome-embedded

938   EVs (N) and the low levels of lysosome-embedded EV production (O) in the N2

939   wildtype worms expressing lysosomal marker LMP-1::GFP, both of which were

940   enhanced by RNAi knockdown of autophagosome formation genes, including *atg-1*,

941   *atg-16.2* and *epg-7*. Each dot represents the number of lysosome-embedded EVs per

942   worm (O). n=180 animals. One-way ANOVA combined with Dunnett's multiple

943   comparisons tests were used for statistical analyses (N and O).

944   **P-V,** Representative TEM images show that the large EVs carry various organelles in

945   the *Is[nhx-2p::CPL-1::wrmScarlet]* strain. (P) A TEM micrograph showing a

946   coelomocyte and the intracellular organelles from the *Is[nhx-2p::CPL-1::wrmScarlet]*

947   worm. (Q, S, U) EVs adjacent to coelomocytes, containing diverse organelles. (R, T, V)

948   Magnified views of the boxed regions in (Q), (S), and (U), respectively. Endoplasmic

949   reticulum fragments (R), mitochondria (T), and Golgi apparatus (V) were identified

950   within the EVs. Purple arrow: endoplasmic reticulum (ER); blue arrow: mitochondria

951   (mito); red arrow: Golgi apparatus (GA).

952   **W,** A schematic illustration of coelomocytes generating purgasomes that export various

953   organelles via ectocytosis. The schematic was created using BioRender.com.

954   All experiments were conducted at least three times. Data are presented as the mean ±

955   SEM.

956

957

Is[nhx-2p::CPL-1::wrmScarlet]

Is[unc-122p::GFP::MCA-3]; Is[nhx-2p::CPL-1::wrmScarlet]

Is[nhx-2p::CPL-1::wrmScarlet]

958

959

960

961

962 **Figure 2: Purgasomes are generated through budding of the plasma membrane**

963 **A-C,** Representative microscopic images showing a forming purgasome, visualized as

964 a plasma membrane bud containing lysosomes labeled with CPL-1::wrmScarlet,

965 originating from the coelomocyte in *Is[nhx-2p::CPL-1::wrmScarlet]* worms. A

966 magnified view of the boxed area in (B) is presented in (C).

967 **D and E,** Micrographs and scatter plot show that *tat-5(RNAi)* enhances purgasome

968 formation induced by the *Is[nhx-2p::CPL-1::wrmScarlet]* transgene. Quantification of

969 purgasome numbers per worm under the indicated treatments is presented in (E).

970 GFP::MCA-3 labels the coelomocyte plasma membrane, while CPL-1::wrmScarlet

971 marks lysosomes. Each dot represents the number of purgasomes per worm (E). n=180

972 animals (E). Two-tailed unpaired t tests were used for statistical analyses (E).

973 **F and G,** Micrographs and scatter plot show that *pad-1(gf, ju1806)* allele reduces

974 cytopurgosis induced by the *Is[nhx-2p::CPL-1::wrmScarlet]* transgene. Quantification

975 of purgasome number is presented in (G). Each dot represents the number of

976 purgasomes per worm (G). n=180 animals. Two-tailed unpaired t tests were used for

977 statistical analyses.

978 All experiments were conducted at least three times. Data are presented as the mean ±

979 SEM.

980

981

982

983

984

985

986

987
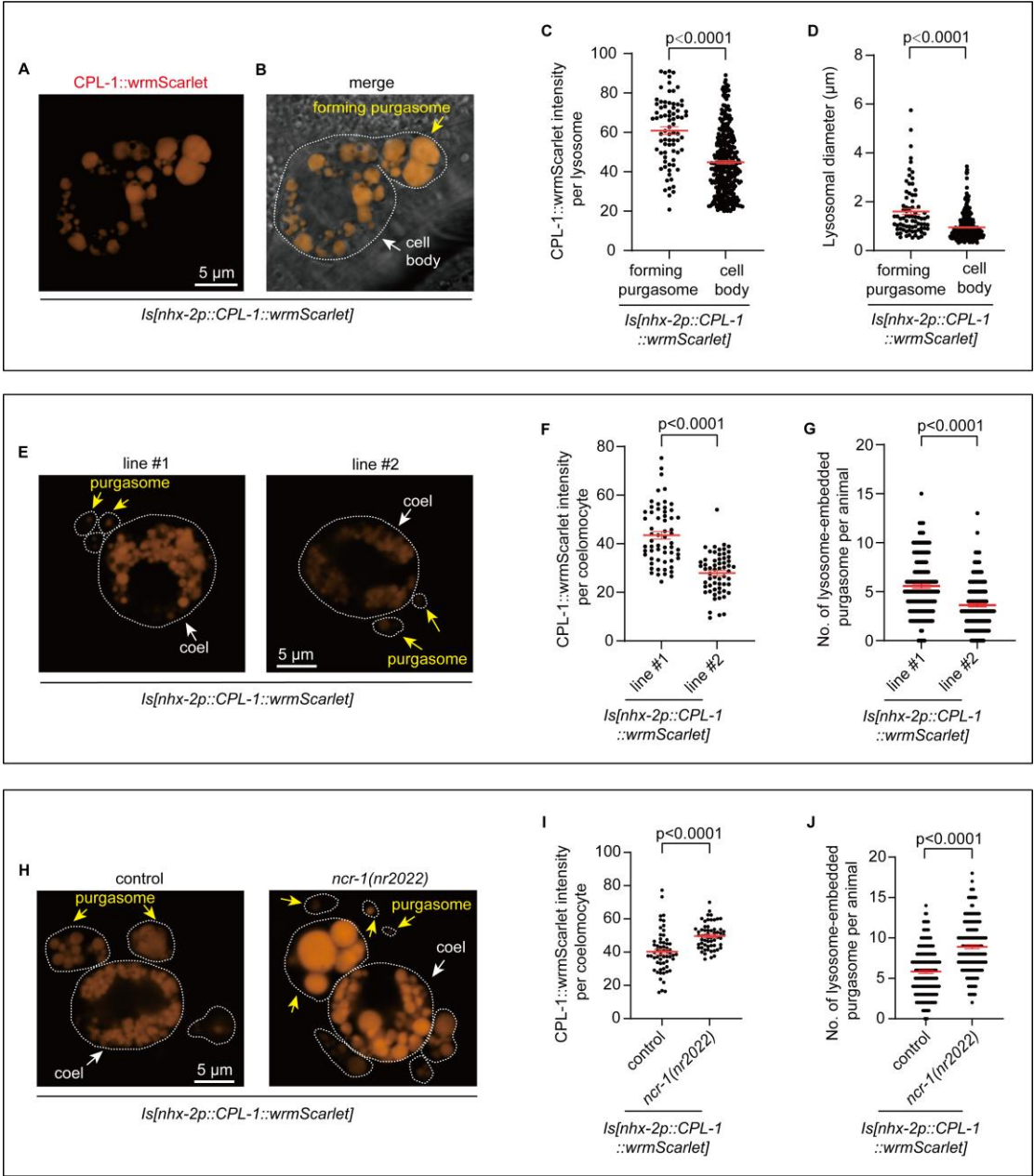
988

989

990

991

992

993

994

995

996   **Figure 3: Lysosomes with impaired degradation capacity are preferentially**

997   **expelled via purgasomes, which respond to the levels of lysosomal overload**

998   **A-D,** Fluorescence micrographs and scatter plots showing larger lysosomal size and

999   stronger accumulation of CPL-1::wrmScarlet in lysosomes within the forming

1000   purgasome compared to those remained in the cell body of coelomocytes in *Is[nhx-*

1001   *2p::CPL-1::wrmScarlet]* worms. Each dot represents the intensity of CPL-

1002   1::wrmScarlet (C) and the diameter of a lysosome (D). n=77 lysosomes in forming

1003   purgasomes or 344 lysosomes in cell bodies from 10 coelomocytes (C and D). Two-

1004   tailed unpaired t tests were used for statistical analyses (C and D).

1005   **E-G,** Representative fluorescence micrographs and quantitative analyses demonstrate

1006   that increased accumulation of CPL-1::wrmScarlet in lysosomes enhances purgasome

1007   production from coelomocytes. Analyses were conducted using two independent lines

1008   of *Is[nhx-2p::CPL-1::wrmScarlet]*, which exhibited varying levels of CPL-

1009   1::wrmScarlet accumulation in lysosomes (E). Each dot represents the intensity of CPL-

1010   1::wrmScarlet in individual coelomocytes (F) and the number of purgasomes per worm

1011   (G). n=60 coelomocytes (F) or 180 animals (G). Two-tailed unpaired t tests were used

1012   for statistical analyses (F and G).

1013   **H-J**, Representative fluorescence micrograph and corresponding quantitative analyses

1014   demonstrate that *ncr-1(nr2022)* increases CPL-1::wrmScarlet accumulation in

1015   lysosomes and enhances purgasome production in *Is[nhx-2p::CPL-1::wrmScarlet]*

1016   worms. Each dot represents the intensity of CPL-1::wrmScarlet in individual

1017   coelomocytes (I) and the number of purgasomes per worm (J). n=60 coelomocytes (I)

1018   or 180 animals (J). Two-tailed unpaired t tests were used for statistical analyses (I and

1019   J).

1020   All experiments were conducted at least three times. Data are presented as the mean ±

1021   SEM.

1022

1023
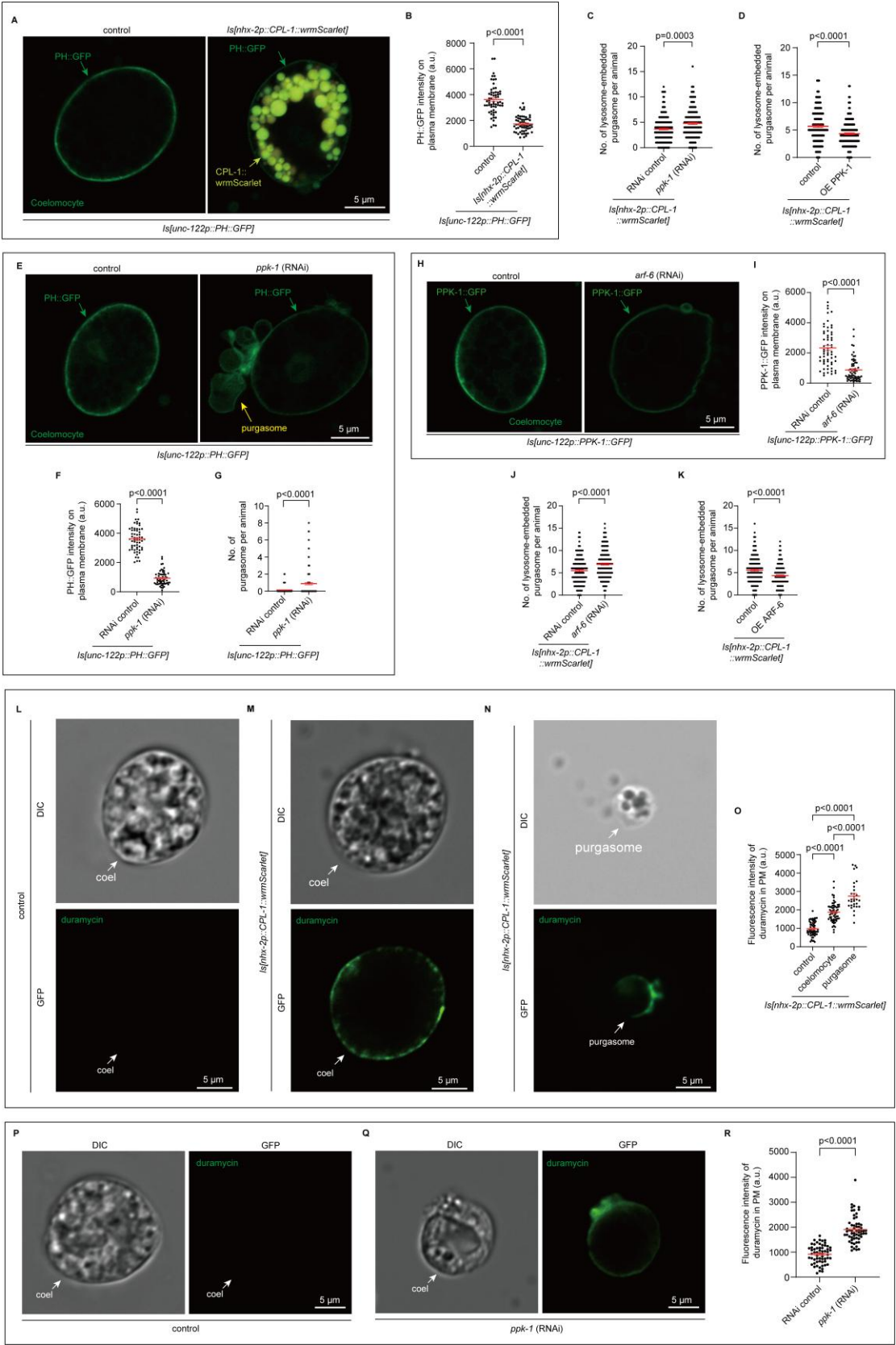
1024

1025

1026

1027 **Figure 4: Lysosomal overload reduces plasma membrane PI(4,5)P$_2$ levels, leading**

1028 **to phosphatidylethanolamine externalization and subsequent promotion of**

1029 **purgasome formation**

1030 **A and B**, Representative fluorescence images and corresponding quantification

1031 showing the reduction of PH::GFP staining on the plasma membrane induced by the

1032 *Is[nhx-2p::CPL-1::wrmScarlet]* transgene. Each dot represents the PH::GFP

1033 fluorescence intensity in the plasma membrane of a coelomocyte in (B). n=60

1034 coelomocytes (B). Two-tailed unpaired t tests were used for statistical analyses (B).

1035 **C and D,** Scatter plot depicting the change in purgasomes number in worms following

1036 *ppk-1* knockdown in *Is[nhx-2p::CPL-1::wrmScarlet] (line #2)* (C) or *ppk-1*

1037 overexpression in *Is[nhx-2p::CPL-1::wrmScarlet] (line #1)* worms (D). Each dot

1038 represents the purgasome count from a single animal. n=180 animals (C and D). Two-

1039 tailed unpaired t tests were used for statistical analyses (C and D).

1040 **E-G**, Microscopic images and corresponding quantitative analyses show a decrease in

1041 PH::GFP fluorescence and an increase in purgasome generation upon *ppk-1* knockdown

1042 in worms lacking CPL-1::wrmScarlet lysosomal accumulation (E). The experiments

1043 were performed in the *Is[unc-122p::PH::GFP]* worms. Each dot represents the

1044 PH::GFP fluorescence intensity on the plasma membrane of a coelomocyte (F) and the

1045 number of purgasomes in a single worm (G). n=60 coelomocytes (F) and 180 animals

1046 (G). Two-tailed unpaired t tests were used for statistical analyses (F and G).

1047 **H and I,** Representative micrograph and corresponding scatter plot showing the

1048 reduction of PPK-1::GFP at the coelomocyte plasma membrane following *arf-6 (RNAi)*

1049 in the N2 wildtype worms expressing *Is[unc-122p::PPK-1::GFP]*. Each dot represents

1050 the PPK-1::GFP intensity measured at the plasma membrane of an individual

1051 coelomocyte. n=60 coelomocytes (I). Two-tailed unpaired t tests were used for

1052 statistical analyses (I).

1053 **J and K,** Scatter plots illustrating an increase in purgasome formation following *arf-6*

1054 knockdown (J), and a decrease in purgasome formation upon *arf-6* overexpression (K)

1055 in *Is[nhx-2p::CPL-1::wrmScarlet]* worms. Each dot represents the number of

1056 purgasomes in a single worm (J and K). n=180 animals (J and K). Two-tailed unpaired

1057 t tests were used for statistical analyses (J and K).

1058 **L-O,** Microscopic images and corresponding quantifications indicate the

1059 externalization of phosphatidylethanolamine, detected by Duramycin staining, on the

1060 plasma membrane of coelomocytes (M) and the purgasome (N) membrane in *Is[nhx-*

1061 *2p::CPL-1::wrmScarlet]* worms. Coelomocytes from N2 wild-type worms served as a

1062 negative control (L). Each dot represents the fluorescence intensity of Duramycin

1063 staining in the membrane of a coelomocyte or a purgasome. n=60 coelomocytes or 30

1064 purgasomes (O). One-way ANOVA combined with Tukey's multiple comparisons tests

1065 were used for statistical analyses (O).

1066 **P-R,** Microscopic images and corresponding quantifications show that

1067 phosphatidylethanolamine is externalized on the plasma membrane of coelomocytes in

1068 N2 wildtype worms treated with *ppk-1(RNAi)*, as detected by Duramycin staining. Each

1069 dot represents the fluorescence intensity of Duramycin staining in the membrane of an

1070 individual coelomocyte from either the control RNAi group or the *ppk-1(RNAi)* group.

1071 n=60 coelomocytes (R). Two-tailed unpaired t tests were used for statistical analyses

1072 (R).

1073 All experiments were conducted at least three times. Data are presented as the mean ±

1074 SEM.

1075

1076

1077

1078

1079

1080

1081

1082
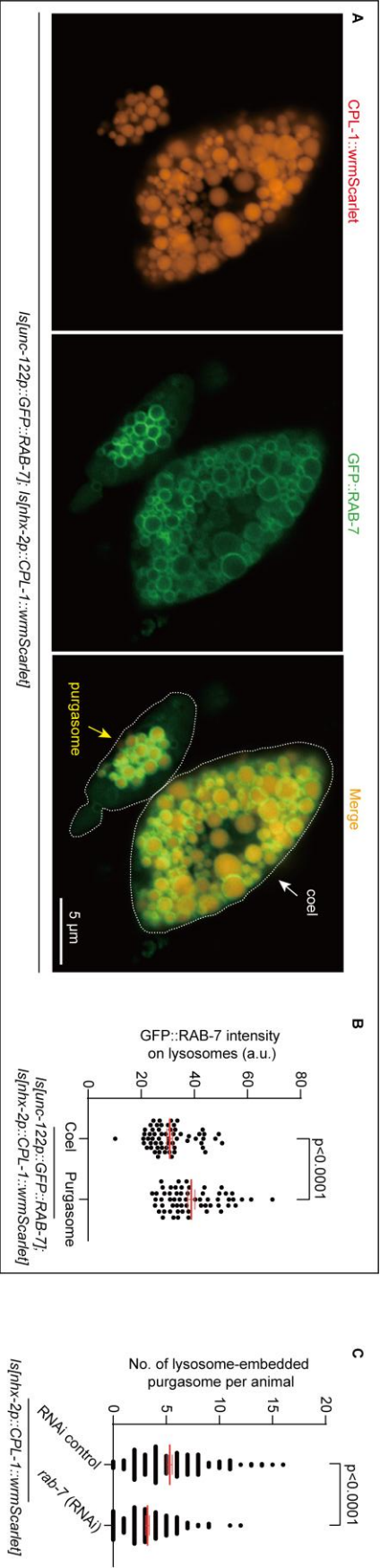
Figure 5: RAB-7 levels on lysosomes determine their sorting into purgasomes

A and B, Fluorescence micrographs and corresponding quantifications show increased localization of GFP::RAB-7 on lysosomes in purgasomes compared to those in coelomocytes of worms expressing *Is[nhx-2p::CPL-1::wrmScarlet]* transgene. Each dot represents the mean GFP::RAB-7 fluorescence intensity in individual purgasomes or coelomocytes (B). n=60 coelomocytes or purgasomes (B). Two-tailed unpaired t tests were used for statistical analyses (B).

C and D, Scatter plots showing that *rab-7* knockdown (C) or expression of a dominant-negative form of *rab-7* in coelomocytes (D) reduced purgasome formation in the worms expressing *Is[nhx-2p::CPL-1::wrmScarlet]* transgene. Each dot represents the number of purgasomes per worm. n=180 animals. Two-tailed unpaired t tests were used for statistical analyses.

E-H, Fluorescence micrographs and corresponding quantifications showing the change in the purgasome formation in the worms with indicated genotypes. Each dot represents the number of purgasomes per worm (H). n=180 animals (H). One-way ANOVA combined with Tukey's multiple comparisons tests were used for statistical analyses (H).

All experiments were conducted at least three times. Data are presented as the mean ± SEM.

1109
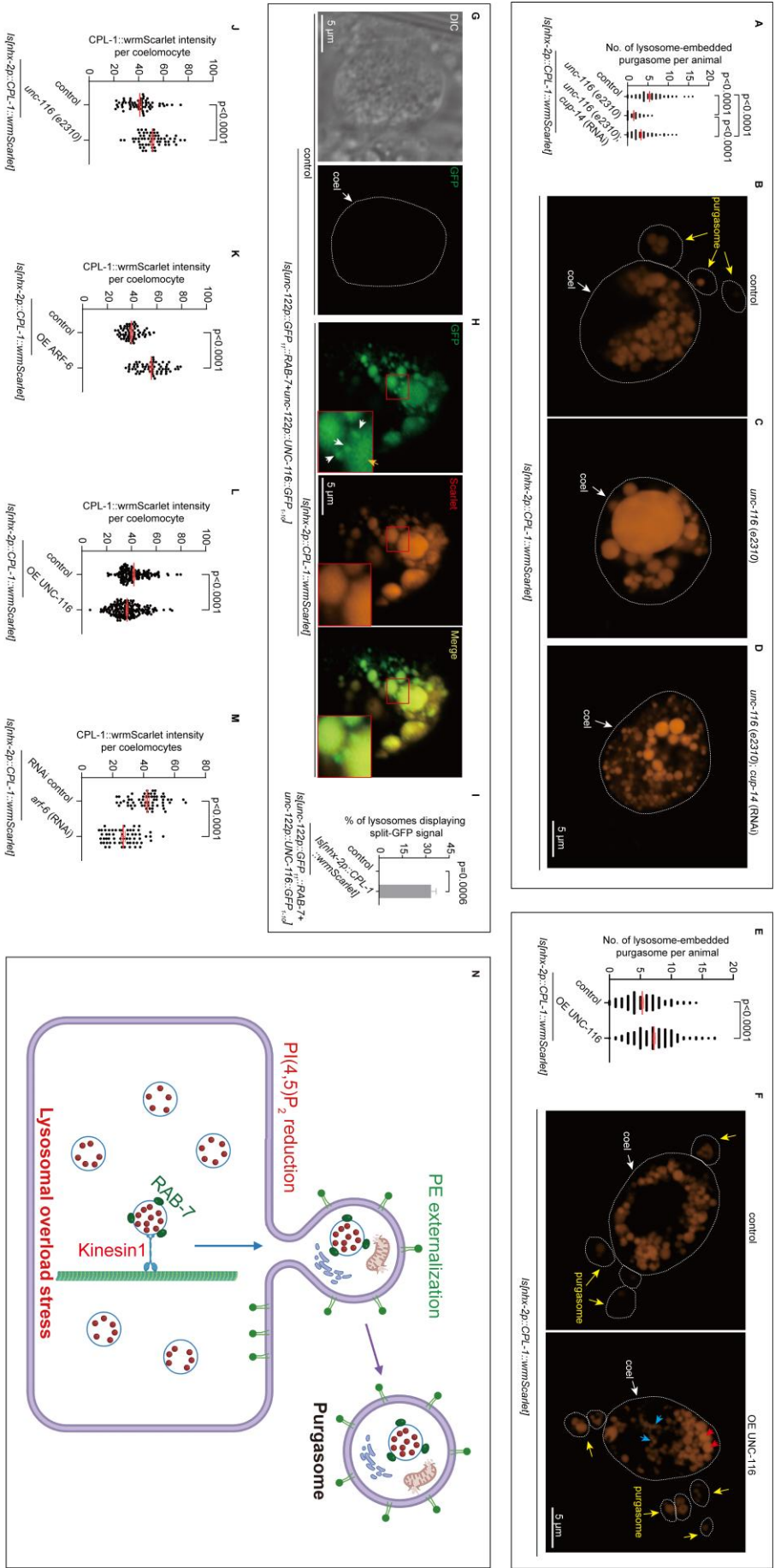
1110 **Figure 6: UNC-116 interacts with RAB-7 to mediate the outward translocation of**

1111 **overloaded lysosomes to the purgasomes, and this lysosomal expulsion maintains**

1112 **lysosomal homeostasis under lysosomal overload stress**

1113 **A-D,** Scatter plots and microscopic images show a reduction in purgasome formation

1114 in *Is[nhx-2p::CPL-1::wrmScarlet]* worms following the introduction of the *unc-*

1115 *116(e2310)* mutation or *unc-116(e2310);cup-14(RNAi)*. Each dot represents the

1116 purgasome count in an individual worm (A). n=180 animals (A). One-way ANOVA

1117 combined with Tukey's multiple comparisons tests were used for statistical analyses

1118 (A).

1119 **E and F,** Scatter plots and microscopic images demonstrate an increase in purgasome

1120 formation from coelomocytes in *Is[nhx-2p::CPL-1::wrmScarlet]* worms following the

1121 overexpression of UNC-116 in the coelomocytes. The overexpression of UNC-116 was

1122 driven by the *unc-122* promoter. Each dot represents the purgasome count in an

1123 individual worm (E). n=180 animals (E). The red and blue arrows indicate lysosomes

1124 located near the cell periphery and in the central region, respectively, showing higher

1125 and lower accumulation of wrmScarlet (F, right panel), which is quantified in Figure

1126 S6F. Two-tailed unpaired t tests were used for statistical analyses (E).

1127 **G-I,** Microscopic images and corresponding quantifications illustrate alterations in the

1128 reconstitution of split-GFP from the transgene *Is[unc-122p::GFP_{11}::RAB-7 + unc-*

1129 *122p::UNC-116::GFP_{1-10}]* in the absence (G) or presence (H) of lysosomal

1130 accumulation of CPL-1::wrmScarlet. White arrow indicates reconstituted split-GFP

1131 fluorescence signal in the presence of *Is[nhx-2p::CPL-1::wrmScarlet]*; yellow arrow

1132 denotes spillover of CPL-1::wrmScarlet fluorescence into the GFP channel in (H). n=30

1133 coelomocytes (I). Two-tailed unpaired t tests were used for statistical analyses (I).

1134 **J-M,** Graphs showing the change in fluorescence intensity of lysosomal-accumulated

1135 CPL-1::wrmScarlet in worms with the indicated genotypes. Lysosomal accumulation

1136 of CPL-1::wrmScarlet in coelomocytes is increased in the presence of *unc-116(e2310)*

1137 mutation (J) or coelomocyte-specific overexpression of ARF-6 (K), and decreased with

1138 coelomocyte-specific overexpression of UNC-116 (L) or *arf-6(RNAi)* (M). The ARF-6

1139   and UNC-116 coelomocyte-specific overexpression are driven by the *Is[unc-122p::ARF-6::GFP]* and *Is[unc-122p::UNC-116::GFP]* transgenes, respectively. Each dot represents the fluorescence intensity of lysosomal-accumulated CPL-1::wrmScarlet in a single coelomocyte. n=60 coelomocytes (J, K, M); n$\geq$146 coelomocytes (L). Two-tailed unpaired t tests were used for statistical analyses (J-M).

1144   **N,** Schematic of the biogenesis mechanism of purgasomes. Cells produce a previously unidentified type of large extracellular vesicle, termed purgasomes, via ectocytosis to export various organelles. Purgasome biogenesis is enhanced in response to lysosomal overload, which reduces plasma membrane levels of $PI(4,5)P_2$ and leads to the externalization of PE, thereby initiating ectocytosis. Overloaded lysosomes are selectively recognized and expelled via purgasomes, which is mediated by RAB-7 and UNC-116/kinesin1, respectively. The schematic was created using BioRender.com.

1151   All experiments were conducted at least three times. Data are presented as the mean $\pm$ SEM.

1153

1154

1155

1156

1157

1158

1159

1160

1161

1162

1163

1164

A Intestinal cell
sp::wrmScarlet expression
conventional secretion
Body cavity
endocytic uptake
lysosome
Coelomocyte

B Is[nhx-2p::sp::wrmScarlet]
DIC + Scarlet
100 µm

C sp::wrmScarlet
LMP-1::GFP
Coelomocyte
4 µm
Is[lmp-1p::LMP-1::GFP];
Is[nhx-2p::sp::wrmScarlet]

D % of sp::wrmScarlet wrapped by LMP-1::GFP
Is[lmp-1p::LMP-1::GFP];
Is[nhx-2p::sp::wrmScarlet]

E LAAT-1::GFP | CPL-1::wrmScarlet | Merge
RNAi control — Intestine
rab-10 (RNAi) — Intestine
5 µm
Is[vha-6p::LAAT-1::GFP]; Is[nhx-2p::CPL-1::wrmScarlet]

F CPL-1::wrmScarlet intensity in intestine
p<0.0001
RNAi control / rab-10 (RNAi)
Is[vha-6p::LAAT-1::GFP];
Is[nhx-2p::CPL-1::wrmScarlet]

G CPL-1::wrmScarlet intensity per coelomocyte
p<0.0001
RNAi control / rab-10 (RNAi)
Is[vha-6p::LAAT-1::GFP];
Is[nhx-2p::CPL-1::wrmScarlet]

H wrmScarlet intensity per coelomocyte
p<0.0001
Is[nhx-2p::CPL-1::wrmScarlet] / Is[nhx-2p::sp::wrmScarlet]

I Scarlet channel | GFP channel | DAPI channel
coel
5 µm
Is[nhx-2p::sp::wrmScarlet]

J coel
EV
5 µm
Is[nhx-2p::CPL-1::wrmScarlet]

K sp::wrmScarlet | GFP::MCA-3 | Merge
coel
EV
5 µm
Is[unc-122p::GFP::MCA-3]; Is[nhx-2p::sp::wrmScarlet]

L % of EVs membrane with GFP::MCA-3 signal
Is[unc-122p::GFP::MCA-3];
Is[nhx-2p::sp::wrmScarlet]

M % of worms with lysosome-embedded vesicle
Is[nhx-2p::sp::wrmScarlet]

N No. of lysosome-embedded vesicle per animal
Is[nhx-2p::sp ::wrmScarlet]

O EV / coel
coel / EV
5 µm
Is[nhx-2p::CPL-1 ::wrmScarlet] | Is[nhx-2p::CPL-1(C144A) ::wrmScarlet]

P wrmScarlet intensity per coelomocyte
p=0.6266
Is[nhx-2p::CPL-1 ::wrmScarlet] / Is[nhx-2p::CPL-1(C144A) ::wrmScarlet]

Q No. of lysosome-embedded vesicle peer animal
p=0.9246
Is[nhx-2p::CPL-1 ::wrmScarlet] / Is[nhx-2p::CPL-1(C144A) ::wrmScarlet]

1165

Figure S1: Purgasome production is enhanced under lysosomal overload stress

A-D, A schematic illustration, microscopic images, and bar graphs demonstrate the conventional secretion of a signal peptide-fused wrmScarlet protein from intestinal cells expressing the transgene *Is[nhx-2p::sp::wrmScarlet]*, followed by uptake by coelomocytes and subsequent lysosomal accumulation. The sp::wrmScarlet protein is specifically expressed in the intestine under the control of the *nhx-2* promoter (A). Microscopic analysis reveals the accumulation of sp::wrmScarlet in coelomocytes (B). Volumetric rendering images and corresponding bar graphs confirm the localization of sp::wrmScarlet within lysosomes of coelomocytes (C and D). Quantitative analysis indicates that sp::wrmScarlet fluorescence is entirely contained within LMP-1-labeled lysosomes. n=30 coelomocytes (D).

E-G, Microscopic images, bar graph and scatter plot indicate that inhibiting lysosomal exocytosis via *rab-10(RNAi)* in *Is[nhx-2p::CPL-1::wrmScarlet]* worms leads to the accumulation of CPL-1::wrmScarlet in intestinal lysosomes (E-F) and a concomitant reduction in its levels in coelomocytes (G). *Is[vha-6p::LAAT-1::GFP]* transgene is used as a marker for intestinal lysosomes. In panel E, fluorescence micrographs show intestinal cells expressing CPL-1::wrmScarlet under normal conditions (upper panel) and after *rab-10* knockdown (lower panel). Panel F presents bar graphs showing that *rab-10* knockdown increases CPL-1::wrmScarlet fluorescence intensity in the intestine. Panel G displays a scatter plot indicating that *rab-10* knockdown decreases CPL-1::wrmScarlet intensity in coelomocytes. Each dot represents the intensity of wrmScarlet in a single coelomocyte (G). n=60 micrographs of intestinal cells (F); n=60 coelomocytes (G). Two-tailed unpaired t tests were used for statistical analyses (F and G).

H, Scatter plot indicates that the wrmScarlet fluorescence intensity in the coelomocytes is significantly higher in *Is[nhx-2p::CPL-1::wrmScarlet]* compared to *Is[nhx-2p::sp::wrmScarlet]*. Each dot represents the intensity of wrmScarlet in a single coelomocyte. n=60 coelomocytes. Two-tailed unpaired t tests were used for statistical analyses.

1195   **I and J,** Multicolor fluorescence imaging revealed that sp::wrmScarlet localized to

1196   coelomocytes without channel bleed-through in the *Is[nhx-2p::sp::wrmScarlet]*

1197   transgenic worm (I), whereas CPL-1::wrmScarlet localized to coelomocytes exhibited

1198   bleed-through into the GFP and DAPI channels in the *Is[nhx-2p::CPL-1::wrmScarlet]*

1199   worm (J). These results indicate a much stronger wrmScarlet signal intensity in the

1200   *Is[nhx-2p::CPL-1::wrmScarlet]* transgenic worms compared to the *Is[nhx-*

1201   *2p::sp::wrmScarlet]* transgenic worms.

1202   **K-N,** Microscopic images and graphs reveal that the *Is[nhx-2p::sp::wrmScarlet]*

1203   transgene triggers the formation of lysosome-embedded EVs from coelomocytes

1204   through ectocytosis. *Is[unc-122p::GFP::MCA-3]* marks the coelomocyte plasma

1205   membrane, and red fluorescence indicates sp::wrmScarlet-labeled lysosomes. All

1206   lysosome-embedded EV membranes are labeled with GFP::MCA-3 derived from the

1207   coelomocyte plasma membrane (K and L). The proportion of *Is[nhx-*

1208   *2p::sp::wrmScarlet]* worms displaying lysosome-embedded EV production is

1209   presented in (M). The number of lysosome-embedded EVs per *Is[nhx-*

1210   *2p::sp::wrmScarlet]* worm is quantified in (N). In (N), each dot represents the number

1211   of purgasomes per worm. n=60 EVs (L); n=180 animals (M and N).

1212   **O-Q,** Microscopic images and scatter plot demonstrate that the accumulation of

1213   wrmScarlet fused to a catalytically inactive form of CPL-1(C144A) in coelomocytes of

1214   *Is[nhx-2p::CPL-1(C144A)::wrmScarlet]* worms results in a level of lysosome-

1215   embedded EVs generation comparable to that observed in *Is[nhx-2p::CPL-*

1216   *1::wrmScarlet]* worms. The two transgenic lines exhibit similar levels of wrmScarlet

1217   fluorescence intensity in coelomocytes (O and P), and no significant differences in

1218   lysosome-embedded EV numbers are detected between *Is[nhx-2p::CPL-1::wrmScarlet]*

1219   and *Is[nhx-2p::CPL-1(C144A)::wrmScarlet]* (Q). In (P), each dot represents the

1220   intensity of wrmScarlet in a single coelomocyte. In (Q), each dot represents the EV

1221   count from a single animal. n=60 coelomocytes (P); n=180 animals (Q). Two-tailed

1222   unpaired t tests were used for statistical analyses (P and Q).

1223   All experiments were conducted at least three times. Data are presented as the mean ±

1224   SEM.

1225

1226

1227

1228

1229

1230

1231

1232

1233
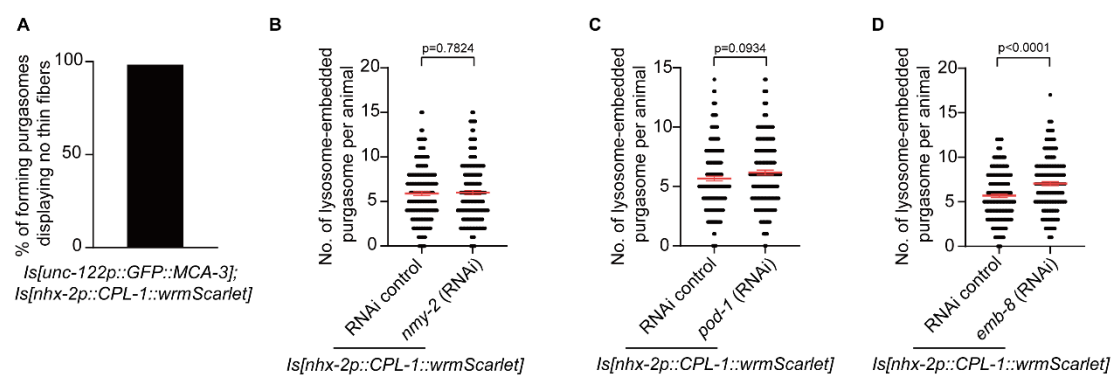
1234

1235

1236

1237

1238

1239

1240

1241

1242

1243

1244

1245

1246

1247

A

% of forming purgasomes displaying no thin fibers

Is[unc-122p::GFP::MCA-3];
Is[nhx-2p::CPL-1::wrmScarlet]

B

No. of lysosome-embedded purgasome per animal

p=0.7824

RNAi control   nmy-2 (RNAi)

Is[nhx-2p::CPL-1::wrmScarlet]

C

No. of lysosome-embedded purgasome per animal

p=0.0934

RNAi control   pod-1 (RNAi)

Is[nhx-2p::CPL-1::wrmScarlet]

D

No. of lysosome-embedded purgasome per animal

p<0.0001

RNAi control   emb-8 (RNAi)

Is[nhx-2p::CPL-1::wrmScarlet]

1248

1249

1250

1251

1252

1253

1254

1255

1256

1257

1258

1259

1260

1261

1262

1263

1264

1265

1266

1267

Figure S2: Purgasomes are distinct from other EVs carrying organelles in their formation mechanisms

A, A bar graph showing that no membranous thin fibers were observed to connect the purgasomes and coelomocytes. n=60 coelomocytes.

B-D, Scatter plots illustrating that knockdown of *nmy-2* (B), *pod-1* (C), or *emb-8* (D) showed either no significant effect (B and C) or a slight increase (D) on purgasome biogenesis in the *Is[nhx-2p::CPL-1::wrmScarlet]* worms. Each dot represents the purgasome count from a single animal. n=180 animals (B-D). Two-tailed unpaired t tests were used for statistical analyses.

All experiments were conducted at least three times. Data are presented as the mean ± SEM.
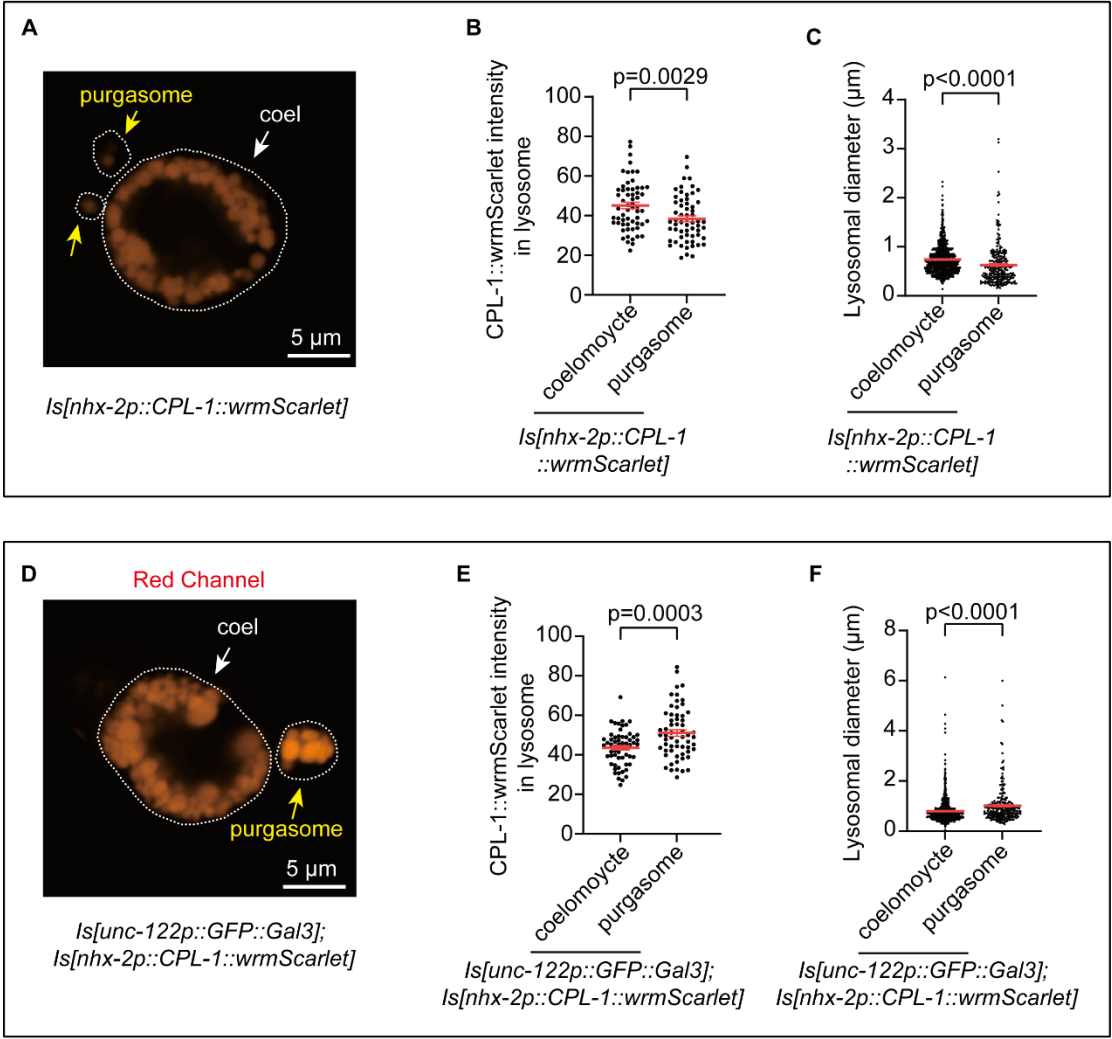
1293

1294
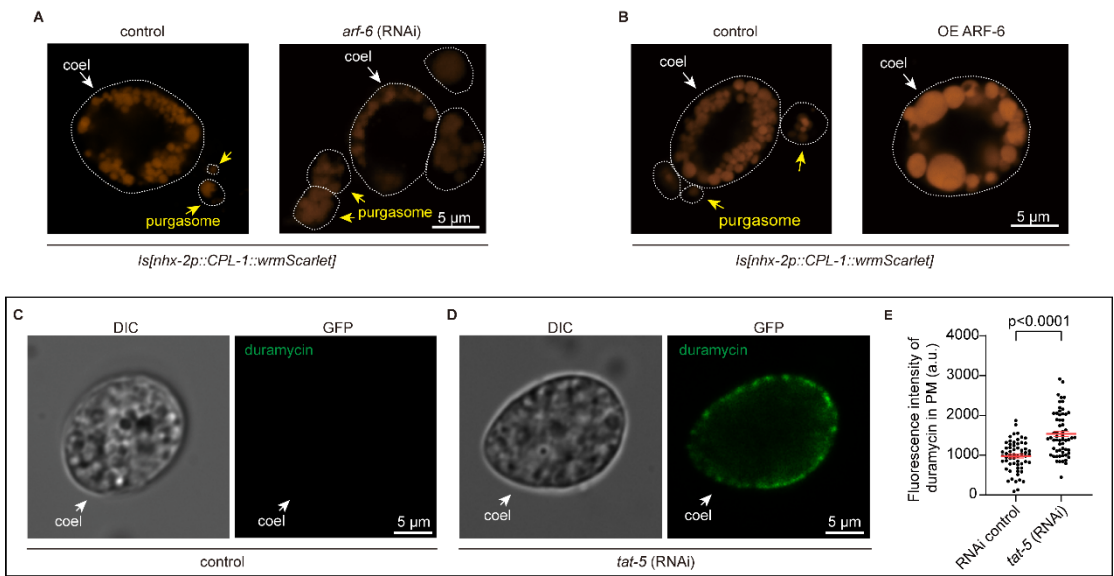
1295

1296

1297

1298

1299

1300

1301

1302

1303

1304

1305

1306 **Figure S3: The lysosomes expelled via purgasomes are leak-prone**

1307 **A-C**, A representative fluorescence micrograph and corresponding quantitative

1308 analyses show that lysosomal size and the accumulation of CPL-1::wrmScarlet in

1309 lysosomes are lower in the released purgasomes than in the coelomocytes in *Is[nhx-*

1310 *2p::CPL-1::wrmScarlet]* worms. Each dot represents the mean intensity of CPL-

1311 1::wrmScarlet in each coelomocyte or purgasome (B) or the size of individual lysosome

1312 measured in either coelomocytes or purgasomes (C). n=60 coelomocytes or purgasomes

1313 (B); n=1103 lysosomes in 30 coelomocytes or 251 lysosomes in 50 purgasomes (C).

1314 Two-tailed unpaired t tests were used for statistical analyses (B and C).

1315 **D-F,** Representative fluorescence micrograph and corresponding quantitative analyses

1316 show that lysosomal size and the accumulation of CPL-1::wrmScarlet in lysosomes are

1317 greater in the released purgasomes than in the coelomocytes in *Is[nhx-2p::CPL-*

1318 *1::wrmScarlet]* worms overexpressing galectin-3. Each dot represents the mean

1319 intensity of CPL-1::wrmScarlet in each coelomocyte (E) or the size of individual

1320 lysosome measured in either coelomocytes or purgasomes (F). n=60 coelomocytes or

1321 purgasomes (E); n=1012 lysosomes in 30 coelomocytes or 247 lysosomes in 41

1322 purgasomes (F). Two-tailed unpaired t tests were used for statistical analyses (E and F).

1323 All experiments were conducted at least three times. Data are presented as the mean ±

1324 SEM.

1325

1326

1327

1328

1329

1330

1331

1332

1333

1334

1335

1336

1337

1338

1339

1340

1341

1342

1343
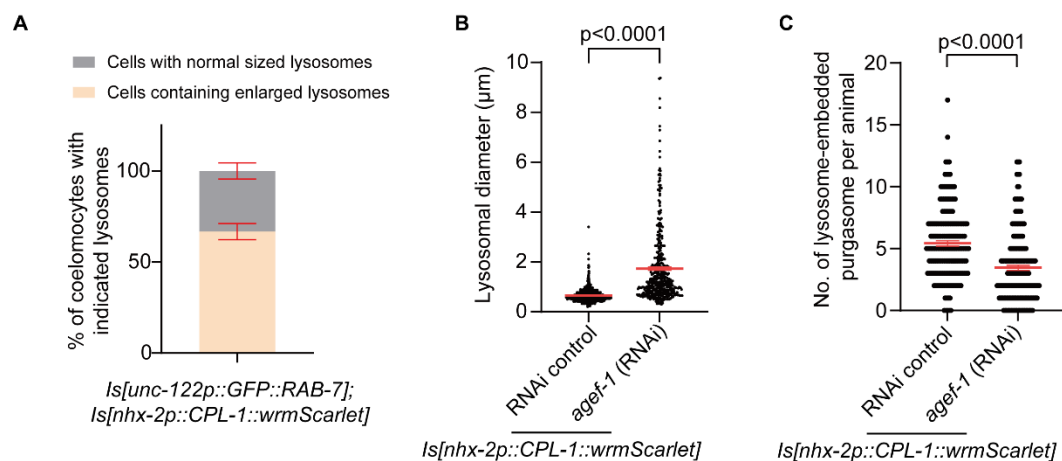
1344

1345

1346

1347

1348

1349

Figure S4: *arf-6* negatively regulates purgasomes generation, and *tat-5* is required for preventing phosphatidylethanolamine externalization

A and B, Representative micrographs showing an increase in purgasome formation after *arf-6* knockdown (A) and a decrease in purgasome formation with *arf-6* overexpression (B) in *Is[nhx-2p::CPL-1::wrmScarlet]* worms, corresponding to the quantifications presented in Figures 4J and 4K, respectively.

C-E, Microscopic images and scatter plots show that phosphatidylethanolamine (PE) is externalized on the plasma membrane of coelomocytes in N2 wildtype worms treated with *tat-5(RNAi)*, as revealed by Duramycin staining. In (E), each data point represents the fluorescence intensity of Duramycin staining in the membrane of an individual coelomocyte from either the control RNAi or the *tat-5(RNAi)*. n=60 coelomocytes (E). Two-tailed unpaired t tests were used for statistical analyses (E).

All experiments were conducted at least three times. Data are presented as the mean ± SEM.

A

Cells with normal sized lysosomes
Cells containing enlarged lysosomes

% of coelomocytes with indicated lysosomes

*Is[unc-122p::GFP::RAB-7];
Is[nhx-2p::CPL-1::wrmScarlet]*

B

Lysosomal diameter (µm)

p<0.0001

RNAi control
agef-1 (RNAi)

Is[nhx-2p::CPL-1::wrmScarlet]

C

No. of lysosome-embedded purgasome per animal

p<0.0001

RNAi control
agef-1 (RNAi)

Is[nhx-2p::CPL-1::wrmScarlet]

1376

1377

1378

1379

1380

1381

1382

1383

1384

1385

1386

1387

1388

1389

1390

1391

1392

1393

1394 **Figure S5: Over-fusion of lysosomes inhibits cytopurgosis**

1395 **A,** Proportion of coelomocytes with or without enlarged lysosomes in the *Is[nhx-*
1396 *2p::CPL-1::wrmScarlet]; Is[unc-122p::GFP::RAB-7]* worms. The diameter of the
1397 largest lysosome in each coelomocyte of *Is[nhx-2p::CPL-1::wrmScarlet]* worms was
1398 quantified and used as the control value. In *Is[nhx-2p::CPL-1::wrmScarlet]; Is[unc-*
1399 *122p::GFP::RAB-7]* worms, a coelomocyte was classified as having enlarged
1400 lysosomes if the diameter of any lysosome exceeded the control lysosome diameter.
1401 n=60 coelomocytes.

1402 **B and C**, graphs demonstrate that *agef-1 (RNAi)* induces lysosomal enlargement and
1403 suppresses purgasome-mediated lysosome expulsion in the *Is[nhx-2p::CPL-*
1404 *1::wrmScarlet]* worms. Each dot represents the diameter of lysosomes within the
1405 coelomocytes (B) and the number of purgasomes per worm (C). n=1708 lysosomes
1406 from 30 coelomocytes (control group) and 449 lysosomes from 30 coelomocytes (*agef-*
1407 *1 RNAi* group) (B). n=180 animals (C). Two-tailed unpaired t tests were used for
1408 statistical analyses.

1409 All experiments were conducted at least three times. Data are presented as the mean ±
1410 SEM.

1411

1412

1413

1414

1415

1416

1417

1418

1419
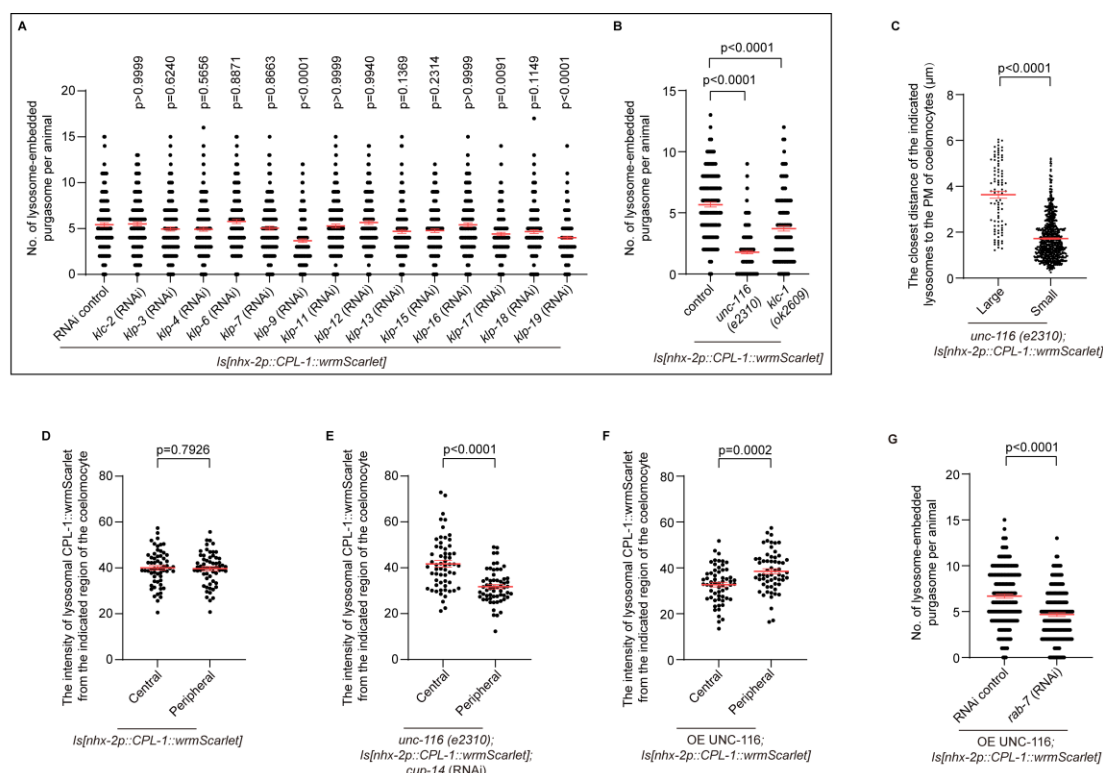
1420

1421

1422

1423

1424

1425

1426

1427

1428

1429

1430

1431

1432

1433

1434 **Figure S6: UNC-116 mediates outward transport of overloaded lysosomes**

1435 **A and B,** Scatter plots illustrating the effect of RNAi or mutations in genes encoding

1436 kinesin on purgasome generation. Each dot represents the number of purgasomes in a

1437 single worm. n=180 animals for each treatment (A and B). One-way ANOVA combined

1438 with Dunnett's multiple comparisons tests were used for statistical analyses (A and B).

1439 **C,** Scatter plot depicting the shortest distance from large or small lysosomes to the

1440 plasma membrane in coelomocytes of *Is[nhx-2p::CPL-1::wrmScarlet]; unc-116(e2310)*

1441 worms. Lysosomes were categorized as large or small based on their diameter relative

1442 to the mean lysosome diameter within the same cell. Those with diameters greater than

1443 the mean were classified as large, while those with diameters smaller than the mean

1444 were classified as small. Each dot represents the distance of a single lysosome to the

1445 plasma membrane. n=91 large lysosomes and 734 small lysosomes in 30 coelomocytes.

1446 Two-tailed unpaired t tests were used for statistical analyses.

1447 **D-F,** Scatter plots depicting the intensity of CPL-1::wrmScarlet in the lysosomes from

1448 the specified regions of the coelomocytes in worms with the indicated genotypes.

1449 Panels D, E, and F present the quantification of the images shown in Figure 6B, 6D,

1450 and the right panel of Figure 6F, respectively. Coelomocytes were approximated as

1451 circular or elliptical regions and subdivided into peripheral and central zones using an

1452 isopleth, a contour line positioned at the radial midpoint between the geometric center

1453 and the boundary perimeter. The CPL-1::wrmScarlet intensity within these defined

1454 regions was then analyzed. In *Is[nhx-2p::CPL-1::wrmScarlet]* worms, the intensity of

1455 CPL-1::wrmScarlet in lysosomes was comparable between the peripheral and central

1456 zones. However, following *unc-116(e2310); cup-14(RNAi)* treatment in the same strain,

1457 the intensity of CPL-1::wrmScarlet in the peripheral lysosomes was lower compared to

1458 that in the central zone. Conversely, upon UNC-116 overexpression, the peripheral

1459 lysosomes exhibited stronger fluorescence than those in the central zone. Each dot

1460 represents the fluorescence intensity of lysosomal-accumulated CPL-1::wrmScarlet in

1461 the indicated region. n=60 coelomocytes (D-F). Two-tailed unpaired t tests were used

1462 for statistical analyses (D-F).

1463 **G,** Scatter plot showing that knockdown of *rab-7* repressed UNC-116-overexpression-

1464 induced increase in purgasome generation. UNC-116 overexpression is driven by the

1465 *Is[unc-122p::UNC-116]* transgene. Each dot represents the purgasome number in one

1466 worm. n=180 animals. Two-tailed unpaired t tests were used for statistical analyses.

1467 All experiments were conducted at least three times. Data are presented as the mean ±

1468 SEM.